Computer Methods in Applied Mechanics and Engineering 450 (2026) 118621

Contents lists available at ScienceDirect

Comput. Methods Appl. Mech. Engrg.

journal homepage: www.elsevier.com/locate/cma

Efficient bound-preserving numerical schemes for a phase-Field model of tumor growth with extracellular matrix degradation

Qiumei Huang [a], Zhonghua Qiao [b], Cheng Wang [c], Huiting Yang [d,a,*]

[a] School of Mathematics, Statistics and Mechanics, Beijing University of Technology, 100124, Beijing, China
[b] Department of Applied Mathematics, The Hong Kong Polytechnic University, Hung Hom, Kowloon, Hong Kong
[c] Department of Mathematics, University of Massachusetts Dartmouth, 02747, North Dartmouth, MA, USA
[d] School of Mathematics and Statistics, Hunan First Normal University, 410205, Changsha, China

ARTICLE INFO

Keywords:
Extracellular matrix degradation
Tumor growth
Phase-field equation
Exponential time differencing Runge-Kutta
Maximum bound principle
Bound preserving.

ABSTRACT

In cancer research, the role of the extracellular matrix (ECM) and its associated matrix-degrading enzyme (MDE) has been a significant area of focus. This study presents a numerical algorithm designed to simulate a previously established tumor model that incorporates various biological factors, including tumor cells, viable cells, necrotic cells, and the dynamics of MDE and ECM. The model consists of a system that includes a phase-field equation, two reaction-diffusion equations, and two ordinary differential equations (ODEs). We employ the fast exponential time differencing Runge-Kutta (ETDRK) method with stabilizing terms to solve this system, resulting in a decoupled, explicit, linear numerical algorithm. The objective of this algorithm is to preserve the physical properties of the model variables, including the maximum bound principle (MBP) for nutrient concentration and MDE volume fraction, as well as bound preserving for ECM density and tumor volume fraction. We perform simulations of 2D and 3D tumor models and discuss how different biological components impact growth dynamics. These simulations may help predict tumor evolution trends, offer insights for related biological and medical research, potentially reduce the number and cost of experiments, and improve research efficiency.

1. Introduction

In 2020, there were an estimated 19.3 million new cancer cases and nearly 10 million cancer deaths worldwide. By 2040, the global cancer burden is expected to reach 28.4 million cases, an increase of 47 % from 2020 [1]. These statistics underscore the importance of cancer research.

The extracellular matrix (ECM) is a complex network of large molecules (such as collagen, enzymes, and glycoproteins) secreted extracellularly, serving primarily as a structural scaffold and biochemical support for cells and tissues. However, the ECM in solid tumors exhibits significant differences from that in normal organs. The ECM often becomes disordered in cases of carcinogenesis. This abnormal ECM can influence cancer progression by directly promoting cell transformation and metastasis [2]. Over the past three to four decades, there has been an exponential increase in the study and recognition of the importance of the matrix in cancer [3]. Numerous investigations have demonstrated that the ECM associated with tumors actively contributes to tumor cell growth, invasion, metastasis, and angiogenesis. Beyond influencing tumor cell behavior, the ECM also indirectly affects drug delivery mechanisms

* Corresponding author.
E-mail addresses: qmhuang@bjut.edu.cn (Q. Huang), zqiao@polyu.edu.hk (Z. Qiao), cwang1@umassd.edu (C. Wang), yanghuiting2022hk@163.com (H. Yang).

https://doi.org/10.1016/j.cma.2025.118621
Received 28 May 2025; Received in revised form 21 November 2025; Accepted 27 November 2025
0045-7825/© 2025 Elsevier B.V. All rights are reserved, including those for text and data mining, AI training, and similar technologies.

[4]. Cancer cells can secrete matrix-degrading enzymes (MDEs) that break down the ECM, allowing cancer cells to breach tissue barriers and spread locally, a critical process in cancer cell invasion. Consequently, matrix degradation is recognized as a fundamental mechanism in tumor development [5]. In recent years, many scientists have devoted considerable efforts to incorporating the ECM into mathematical models of tumors. A reaction-diffusion partial differential equation system was used in [6] to simulate the interactions among cancer cells, the ECM, and MDE. A system of five coupled partial differential equations was established by [7] to describe the dynamics and interactions of cancer cells, collagen fibers, and the enzymes MMP and lysyl oxidase (LOX), with the objective of better understanding cancer cell migration through ECM remodeling. A multiscale hybrid system composed of partial differential equations and stochastic differential equations was constructed by [8], describing the evolution of epithelial cells (ECs) and mesenchymal-like cells (MCs), to simulate the combined invasion of the ECM by two types of cancer cells (the ECs and the MCs). Tumor growth towards lower ECM conductivity regions under Darcy's law and steady morphology was discussed in [9] as well. Blanco et al. [10] developed a multiscale mathematical model in which tumors are represented as poroelastic materials composed of interstitial fluid and solid components (tumor cells, healthy cells, and ECM), with mechanical behavior governed by their elastic properties.

Phase-field equations have become increasingly popular in mathematical modeling of tumors, offering advantages such as the ability to describe complex interface dynamics and handle multiscale problems. Wu et al. [11] considered a diffuse-interface tumor growth system consisting of a reactive Cahn-Hilliard equation and a reaction-diffusion equation. They employed finite element spatial discretization and a modification of the Crank-Nicolson method as time discretization. Xu et al. [12,13] considered a model composed of two coupled compartments: cellular growth model using the phase-field approach, and the chemical transport model using standard diffusion-reaction equations. Subsequently, they proposed a phase-field model of vascular tumor growth integrated with imaging data. Lorenzo et al. [14] developed a phase-field model of prostate tumor growth coupled with reaction-diffusion equations, solved using present algorithms for local h-adaptivity of hierarchical B-splines to be utilized in isogeometric analysis. Colli et al. [15] proposed a phase-field model of prostate cancer growth incorporating chemotherapy and antiangiogenic therapy effect. The isogeometric analysis (IGA) is used as the spatial discretization, while a generalized-α method is employed as the temporal discretization. The phase-field Cahn-Hilliard equation and tumor growth models were simulated in [16], using a second-order semi-implicit backward differential formula with a stabilized term in the time discretization, and the element-free Galerkin method for spatial discretization. J. Tinsley Oden and collaborators have extensively studied tumor growth dynamics through phase-field modeling, considering multiple biological and mechanical factors influencing tumor development and invasion [17–21]. These studies have employed finite element methods for spatial discretization and semi-implicit algorithms for time discretization.

In recent years, the numerical design has increasingly focused on preserving the physical properties of the original models. The preservation of the maximum bound principle (MBP) and bound preserving has attracted significant attention from researchers, making it a hot research topic in the field of computational mathematics. Ju et al. [22] developed time integration schemes for semilinear parabolic equations that preserve the high-order MBP, utilizing the integrating factor Runge-Kutta (IFRK) method. Feng et al. [23] presented a modified Leap-Frog finite difference scheme for the Allen-Cahn equation, which is linear second-order, maximum-principle preserving, and unconditionally energy-stable. Furthermore, for Allen-Cahn equations, Zhang et al. [24,25] introduced explicit, large time-stepping algorithms that maintain fixed-points and maximum principle for any time step size, and a high-order maximum-principle-preserving framework. In particular, Du et al. [26,27] introduced a framework that allows for the analysis of the MBP in the context of semilinear parabolic equations and proposed schemes for exponential time differencing (ETD) that unconditionally preserve the MBP. Given the importance of physical structure-preserving properties in the numerical simulations, this study also aims to construct schemes that preserve the MBP and bound preserving specifically for tumor growth models. In our previous research [28], we successfully developed a second-order exponential time-differencing Runge-Kutta (ETDRK) method that numerically ensures the MBP for the tumor phase-field variable and the non-negativity of two concentration variables. The constructed algorithm effectively simulates the growth of prostate cancer (PCa) and its response to drug treatment.

The primary contributions of this study are threefold. First, recognizing that many numerical schemes for complex tumor models rely on cut-off operators to maintain physical bounds, we develop an ETD scheme and prove that the numerical scheme adheres to the MBP and boundedness over the spatial domain and time interval of the simulations. Second, the proposed schemes are efficient, explicit, and linearly decoupled, enabling the effective use of fast solvers in large-scale simulations. Third, we also simulated tumor evolution under different initial ECM conditions and analyzed how various biological components affect the growth dynamics of the system through different parameter settings. These simulation results contribute to a deeper understanding of the tumor growth process and offer insights that may assist in predicting tumor growth.

The structure of this paper is organized as follows. In Section 2, the tumor growth model is reviewed. In Section 3, we introduce fully discrete schemes and prove that these schemes satisfy the discrete MBP and ensure discrete bound preservation. In Section 4, the numerical simulations of 2D and 3D tumor growth models are presented. Finally, the main achievements of this study are summarized, and potential future research directions are discussed in Section 5.

2. Model review

This section provides an overview of the mathematical model of tumor growth under investigation, presenting a phase-field approach to tumor growth that incorporates the degradation of the ECM. This model, a simplified version of the original model in Fritz et al. [18], employs a fourth-order phase-field equation to capture tumor dynamics. It also includes two reaction-diffusion equations for critical nutrients and MDE. The behavior of necrotic tumor cells and the ECM are represented through two partial differential equations (PDEs) that reduce to ordinary differential equations (ODEs) at each spatial point.

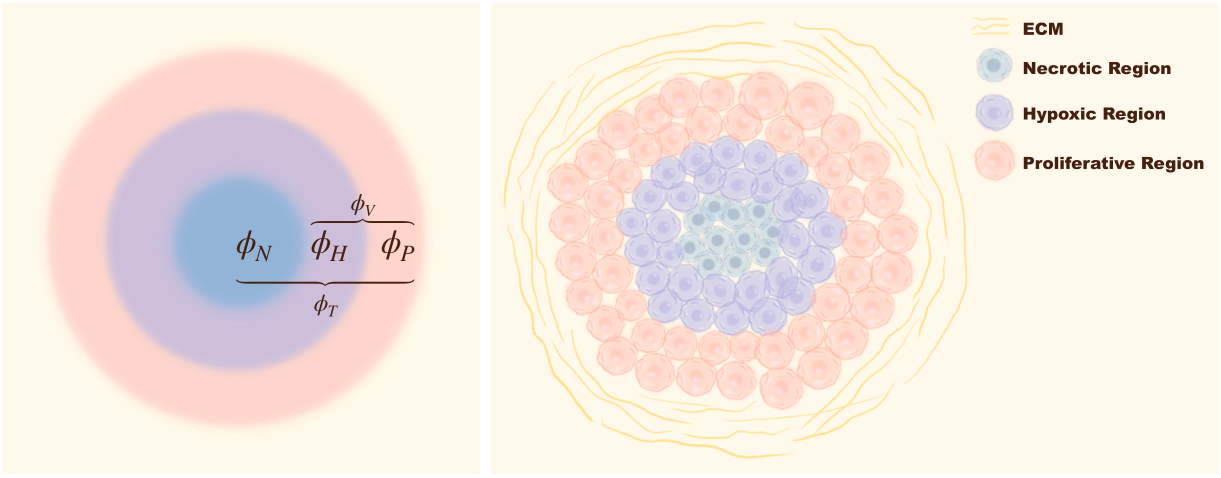

Fig. 1. Schematic of tumor spatial organization and layered cell structure.

2.1. Total tumor cells dynamics

In the area of tumor modeling, tumors are conventionally segregated into three distinct regions [29], as illustrated in Fig. 1(a). These regions encompass the proliferative region, the hypoxic region, and the necrotic region, represented by the volume fractions ϕ_P, ϕ_H, and ϕ_N, respectively. Therefore, the total volume fraction of tumor cells, ϕ_T, can be expressed as the sum of these three components, that is, $\phi_T = \phi_P + \phi_H + \phi_N$. As illustrated in Fig. 1(b), the outer layer, known as the proliferative region, is characterized by cells that have a high propensity to mitosis due to sufficient nutrients, thus fueling tumor growth. The middle layer, or the hypoxic region, is populated by cells that are in a state of hypoxia due to nutrient insufficiency, rendering them incapable of proliferation. The innermost layer, called the necrotic region, is where cells have succumbed to nutrient deficiency, primarily due to the difficulty in nutrient penetration into the tumor core. The aforementioned modeling method for tumors is highly popular in the literature on numerical simulations of cancer dynamics [12,13,29], providing a clearer understanding of the structure and composition of the tumor. Considering that both the proliferative and hypoxic regions consist of viable cells, we are able to express the volume fraction of these viable tumor cells, ϕ_V, as the sum of ϕ_P and ϕ_H, that is, $\phi_V = \phi_T - \phi_N$. All volume fraction variables ϕ_T, ϕ_V, ϕ_N have to be within the range $[0, 1]$. Moreover, the necrotic tumor cells volume fraction ϕ_N should be less than or equal to the total tumor volume fraction ϕ_T.

The dynamics of ϕ_T are dictated by several factors. The growth of the tumor adheres to a logistic model, with a proliferation rate λ_T^{pro}. The volume fraction of total tumor cells can experience a decrease due to the natural apoptosis of viable cells, occurring at a rate denoted by λ_T^{apo}, which is a non-negative constant. Consequently, the evolution equation for ϕ_T is expressed as the following phase-field equation:

$$\partial_t \phi_T = \operatorname{div} J - \operatorname{div} J_\alpha + \lambda_T^{\text{pro}} \phi_\sigma \phi_V \left(1 - \phi_T\right) - \lambda_T^{\text{apo}} \phi_V. \tag{2.1}$$

In this equation, J is the mass flux and J_α is the adhesion flux, representing the influx of tumor mass due to the haptotaxis effect. The mass flux J is given by

$$J = m_T\left(\phi_V\right) \nabla \mu, \tag{2.2}$$

where $m_T\left(\phi_V\right)$ is the cell mobility matrix defined as $m_T\left(\phi_V\right) = M_T \phi_V^2 \left(1 - \phi_V\right)^2$ with $M_T > 0$. The chemical potential μ is defined as

$$\mu = \Psi'\left(\phi_T\right) - \varepsilon_T^2 \Delta \phi_T, \tag{2.3}$$

in which Ψ is a double-well potential, given by $\Psi\left(\phi_T\right) = \bar{E} \phi_T^2 \left(1 - \phi_T\right)^2$ with $\bar{E} > 0$, and ε_T is a positive parameter associated with surface energy.

Finally, the adhesion flux, denoted as J_α, represents a local gradient-based haptotaxis effect [30,31], and is defined as

$$J_\alpha\left(\phi_V, \theta\right) = \chi_H \phi_V \nabla \theta, \tag{2.4}$$

where χ_H represents the haptotaxis parameter and θ is the density of ECM (discussed in Section 2.5).

2.2. Necrotic tumor cell dynamics

The volume fraction of necrotic tumor cells, ϕ_N, is assumed to be non-diffusive, meaning that it evolves over time but does not spread through spatial diffusion. Its dynamics are described by the following equation:

$$\partial_t \phi_N = \lambda_{VN} \mathcal{H}(\sigma_{VN} - \phi_\sigma)\phi_V. \tag{2.5}$$

Here, ϕ_σ represents the nutrient concentration, which varies dynamically in both space and time, due to the diffusion process and consumption. The non-negative parameter λ_{VN} controls the rate at which viable tumor cells transform into necrotic cells. Meanwhile, the Heaviside step function, $\mathcal{H}$ is defined as:

$$\mathcal{H}(x) := \begin{cases} 1, & x \geq 0, \\ 0, & x < 0. \end{cases} \tag{2.6}$$

In Eq. (2.5), $\mathcal{H}$ acts as a "switch" that regulates necrotic cell formation based on the local nutrient concentration ϕ_σ. Specifically, when ϕ_σ drops below the threshold value σ_{VN}, $\mathcal{H}(\sigma_{VN} - \phi_\sigma)$ is activated (equals 1), causing an increase in ϕ_N. This reflects the biological process where insufficient nutrient supply leads to cell death and an expansion of the necrotic region.

Moreover, the necrotic tumor cells volume fraction ϕ_N should be less than or equal to the total tumor volume fraction ϕ_T, and all volume fraction variables ϕ_T, ϕ_V, ϕ_N have to be within the range $[0, 1]$.

2.3. Critical nutrient dynamics

The nutrient concentration, denoted as ϕ_σ, includes substances such as oxygen or glucose. In this model, the nutrient concentration decreases as it is consumed by viable tumor cells at a positive constant consumption rate λ_σ. For our simulations, we set $\lambda_\sigma = 1.5$. The nutrient concentration $\phi_\sigma = \phi_\sigma(x, t)$ is dictated by a reaction-diffusion equation:

$$\partial_t \phi_\sigma = \frac{M_\sigma}{\delta_\sigma} \Delta \phi_\sigma - \lambda_\sigma \phi_V \phi_\sigma, \tag{2.7}$$

where δ_σ and M_σ are the respective positive constants associated with nutrient diffusion and mobility. It should be noted that the nutrient concentration ϕ_σ is non-negative and cannot exceed its initial maximum value $|\phi_\sigma^0|_{\max}$, since nutrients are consumed without external supply.

2.4. MDE dynamics

When the local supply of nutrients ϕ_σ drops below a certain threshold, tumor cells can produce MDEs that facilitate cell migration by degrading the ECM. The MDE production rate by viable cells is directly proportional to the nutrient concentrations and the density of ECM, with a rate represented by λ_M^{pro}. Following the modeling assumption in [18], we introduce the factor $\frac{\sigma_H}{\sigma_H + \phi_\sigma}$ (where $\sigma_H > 0$ is the hypoxia threshold) in the source term to reflect the fact that MDE production is enhanced under low-nutrient [32] and high-ECM conditions. The MDEs decrease due to a natural decay process at a rate of λ_M^{dec}, and are also consumed in the ECM degrading process, which occurs at a rate of $\lambda_\theta^{\text{dec}}$. The volume fraction of MDE ϕ_M is dictated by the following equation:

$$\partial_t \phi_M = M_M \Delta \phi_M - \lambda_M^{\text{dec}} \phi_M + \lambda_M^{\text{pro}} \phi_V \theta \frac{\sigma_H}{\sigma_H + \phi_\sigma}(1 - \phi_M) - \lambda_\theta^{\text{dec}} \theta \phi_M, \tag{2.8}$$

where M_M is a positive constant associated with the mobility. The volume fraction of MDE, ϕ_M, should be constrained within the interval $[0, 1]$.

2.5. ECM dynamics

The density of the ECM θ is another variable assumed to be non-diffusive in the model. Its evolution reflects the degradation of ECM caused by specific MDEs. The degradation rate of ECM is controlled by the parameter $\lambda_\theta^{\text{deg}}$. The dynamics of θ are governed by the following equation:

$$\partial_t \theta = -\lambda_\theta^{\text{deg}} \theta \phi_M. \tag{2.9}$$

Since the model does not account for ECM generation, θ is always constrained by $0 \leq \theta \leq |\theta^0|_{\max}$, meaning that its density cannot exceed the initial maximum value and remains non-negative throughout the degradation process.

2.6. The coupled tumor growth system

Summarizing the previous sections, the model describes tumor progression by incorporating multiple interacting components, including the total volume fraction of tumor cells ϕ_T, the volume fraction of necrotic tumor cells ϕ_N, the nutrient concentration ϕ_σ,

Table 1
Parameter values involved in the model.

Parameter	Value	Parameter	Value
ϵ_T	0.005	χ_H	0.001
$\bar{E}$	0.045	λ_T^{pro}	2
δ_σ	0.01	λ_T^{apo}	0.005
λ_σ	1.5	λ_{VN}	1
M_σ	0.001	λ_M^{pro}	1
M_T	2	λ_M^{dec}	1
M_M	0.1	$\lambda_\theta^{\text{deg}}$	1
σ_{VN}	0.44	$\lambda_\theta^{\text{dec}}$	0.1
σ_H	0.6		

the volume fraction of MDEs ϕ_M, and the density of the ECM θ. Ultimately, we obtain the following coupled governing system:

$$\begin{cases} \partial_t \phi_T = \operatorname{div}(m_T(\phi_V)\nabla\mu) - \operatorname{div} J_\alpha(\phi_V,\theta) + \lambda_T^{\text{pro}}\phi_\sigma\phi_V(1-\phi_T) - \lambda_T^{\text{apo}}\phi_V, \\ \quad \mu = \bar{E}(4\phi_T^3 - 6\phi_T^2 + 2\phi_T) - \epsilon_T^2\Delta\phi_T, \\ \partial_t \phi_N = \lambda_{VN}\mathcal{H}(\sigma_{VN} - \phi_\sigma)\phi_V, \\ \partial_t \phi_\sigma = \dfrac{M_\sigma}{\delta_\sigma}\Delta\phi_\sigma - \lambda_\sigma\phi_V\phi_\sigma, \\ \partial_t \phi_M = M_M\Delta\phi_M - \lambda_M^{\text{dec}}\phi_M + \lambda_M^{\text{pro}}\phi_V\theta\dfrac{\sigma_H}{\sigma_H+\phi_\sigma}(1-\phi_M) - \lambda_\theta^{\text{dec}}\theta\phi_M, \\ \partial_t \theta = -\lambda_\theta^{\text{deg}}\theta\phi_M. \end{cases} \tag{2.10}$$

with the following initial and homogeneous Neumann boundary conditions, which ensure the steady-state distribution of the model variables at the boundary:

$$\begin{aligned} &\phi_T(0) = \phi_{T,0},\ \phi_\sigma(0) = \phi_{\sigma,0},\ \phi_M(0) = \phi_{M,0},\ \phi_N(0) = \phi_{N,0},\ \theta(0) = \theta_0, \quad \text{in } \Omega, \\ &\frac{\partial\phi_T}{\partial\mathbf{n}} = \frac{\partial\phi_\sigma}{\partial\mathbf{n}} = \frac{\partial\phi_M}{\partial\mathbf{n}} = m_T(\phi_V)\frac{\partial\mu}{\partial\mathbf{n}} - J_\alpha(\phi_V,\theta)\cdot\mathbf{n} = 0, \quad \text{on } [0,T]\times\partial\Omega, \end{aligned} \tag{2.11}$$

where Ω is a bounded domain within the d-dimensional real space $\mathbb{R}^d$, $d = \{2,3\}$, with a Lipschitz continuity on the boundary. Moreover, $\mathbf{n}$ represents the outward unit normal vector on the boundary, and $T > 0$ represents the final time.

To approximate the Heaviside step function, different smooth functions can be used. Here, we employ a smooth function, as delineated in [33], to approximate the Heaviside step function (2.6),

$$\mathcal{H}(x) = \frac{1}{2}\left(1 + \frac{2}{\pi}\arctan\left(\frac{x}{\epsilon_1}\right)\right). \tag{2.12}$$

In the simulations, we set $\epsilon_1 = 1e-3$. Alternatively, a sigmoid function can also be used [18] for this approximation.

To ensure that ϕ_T falls within the range of $[0,1]$, we employ a cut-off operator $\mathscr{C}(\phi_T)$

$$\mathscr{C}(\phi_T) = \max(0, \min(1, \phi_T)). \tag{2.13}$$

In turn, ϕ_V is substituted into the original equation with

$$\phi_V = \mathscr{C}(\phi_T) - \phi_N. \tag{2.14}$$

Table 1, shown below, contains all the dimensionless parameter values pertinent to this model system, selected based on reference [18].

3. The numerical method

In this section, we propose decoupled and efficient numerical schemes, based on the ETD approach, to solve the coupled tumor growth model (2.10).

We set the time step size as $\tau = T/N_t$, where $t_n = n\tau$ for $n = 0,\dots,N_t$. The design of numerical schemes should also present the properties of the MBP for the nutrient concentration and MDE volume fraction, as well as the bound preservation for the ECM density and tumor volume fraction, that is,

(i). For total tumor and necrotic core volume fractions: $0 \le \phi_N(\cdot,t_n) \le \phi_T(\cdot,t_n) \le 1$.
(ii). For nutrient concentration: $\phi_\sigma(\cdot,t_n) \in [0, |\phi_\sigma^0|_{\max}]$.
(iii). For MDE volume fraction: $\phi_M(\cdot,t_n) \in [0,1]$.
(iv). For ECM density: $\theta(\cdot,t_n) \in [0, |\theta^0|_{\max}]$.

In this section, we use the central finite difference scheme for spatial discretization and choose the ETDRK method and trapezoidal rule for temporal discretization. Additionally, fast computations based on FFT are employed to enhance computational efficiency.

After applying a cut-off operator to the updated ϕ_T at each time step, we prove that the ETDRK method preserves the boundedness of ϕ_σ and ϕ_M. For ϕ_N and θ, the trapezoidal rule ensures their boundedness under appropriate time step choices (which can be readily satisfied).

3.1. Two-dimensional spatial discretization

For spatial discretization, we apply the central finite difference approximation, using the notation and results for some discrete functions and operators as described in [34,35]. A rectangular domain Ω is considered, defined by $x \in (-1,1)$ and $y \in (-1,1)$, where $h_x = 2/m_x$ and $h_y = 2/n_y$, with m_x and n_y being positive integers. The numerical solutions are denoted as $\phi_{T\,i,j}(t) \approx \phi_T(x_i, y_j, t)$, $\phi_{\sigma\,i,j}(t) \approx \phi_\sigma(x_i, y_j, t)$, and $\phi_{M\,i,j}(t) \approx \phi_M(x_i, y_j, t)$, applicable for $0 \le i \le m_x$ and $0 \le j \le n_y$.

Consider the following three sets:

$$E_m = \{-1 + i \cdot h_x \mid i = 0, \dots, m_x\},$$
$$C_m = \left\{-1 + (i - \frac{1}{2}) \cdot h_x \,\middle|\, i = 1, \dots, m_x\right\},$$
$$C_{\tilde{m}} = \left\{-1 + (i - \frac{1}{2}) \cdot h_x \,\middle|\, i = 0, \dots, m_x + 1\right\}.$$

The points in set E_m are called edge-centered points, while the points in sets C_m and $C_{\tilde{m}}$ are referred to as cell-centered points. The points in the set $C_{\tilde{m}} \backslash C_m$ are the ghost points. Similar notations could be introduced for the sets E_n, C_n, and $C_{\tilde{n}}$.

Define the function spaces as follows:

$$\begin{aligned} C_{m\times n} &= \{\phi : C_m \times C_n \to \mathbf{R}\}, & C_{\tilde{m}\times\tilde{n}} &= \{\phi : C_{\tilde{m}} \times C_{\tilde{n}} \to \mathbf{R}\},\\ C_{\tilde{m}\times n} &= \{\phi : C_{\tilde{m}} \times C_n \to \mathbf{R}\}, & C_{m\times\tilde{n}} &= \{\phi : C_m \times C_{\tilde{n}} \to \mathbf{R}\},\\ \mathcal{E}^{\mathrm{ew}}_{m\times n} &= \{f : E_m \times C_n \to \mathbf{R}\}, & \mathcal{E}^{\mathrm{ns}}_{m\times n} &= \{f : C_m \times E_n \to \mathbf{R}\}. \end{aligned}$$

The functions of $C_{m\times n}, C_{\tilde{m}\times n}, C_{m\times\tilde{n}}$, and $C_{\tilde{m}\times\tilde{n}}$ are called the cell-centered functions. These functions are characterized by $\phi_{i,j} := \phi(x_i, y_j)$, where $x_i = -1 + (i - \frac{1}{2}) \cdot h_x, y_j = -1 + (j - \frac{1}{2}) \cdot h_y$, with i and j taking integer and half-integer values.

The functions of $\mathcal{E}^{\mathrm{ew}}_{m\times n}$ and $\mathcal{E}^{\mathrm{ns}}_{m\times n}$ are known as east-west and north-south edge-centered functions. The east-west edge-centered functions are denoted by $f_{i+\frac{1}{2},j} := f(x_{i+\frac{1}{2}}, y_j)$, and the north-south edge-centered functions are denoted by $f_{i,j+\frac{1}{2}} := f(x_i, y_{j+\frac{1}{2}})$.

The operators $d_x : \mathcal{E}^{\mathrm{ew}}_{m\times n} \to C_{m\times n}$ and $d_y : \mathcal{E}^{\mathrm{ns}}_{m\times n} \to C_{m\times n}$ are defined component-wise as edge-to-center difference operators:

$$d_x f_{i,j} = \frac{1}{h_x}\left(f_{i+\frac{1}{2},j} - f_{i-\frac{1}{2},j}\right), \quad d_y f_{i,j} = \frac{1}{h_y}\left(f_{i,j+\frac{1}{2}} - f_{i,j-\frac{1}{2}}\right), i = 1, \dots, m_x, j = 1, \dots, n_y.$$

The center-to-edge average and difference operators:

$$A_x\phi_{i+\frac{1}{2},j} = \frac{1}{2}\left(\phi_{i,j} + \phi_{i+1,j}\right), \quad D_x\phi_{i+\frac{1}{2},j} = \frac{1}{h_x}\left(\phi_{i+1,j} - \phi_{i,j}\right), i = 0, \dots, m_x, j = 1, \dots, n_y,$$

$$A_y\phi_{i,j+\frac{1}{2}} = \frac{1}{2}\left(\phi_{i,j} + \phi_{i,j+1}\right), \quad D_y\phi_{i,j+\frac{1}{2}} = \frac{1}{h_y}\left(\phi_{i,j+1} - \phi_{i,j}\right), i = 1, \dots, m_x, j = 0, \dots, n_y,$$

where A_x, D_x: $C_{\tilde{m}\times n} \to \mathcal{E}^{\mathrm{ew}}_{m\times n}$, and A_y, D_y: $C_{m\times\tilde{n}} \to \mathcal{E}^{\mathrm{ns}}_{m\times n}$.

The discrete gradient $\nabla_h : C_{\tilde{m}\times\tilde{n}} \to \vec{\mathcal{E}}_{m\times n} := \mathcal{E}^{\mathrm{ew}}_{m\times n} \times \mathcal{E}^{\mathrm{ns}}_{m\times n}$ is defined via

$$\nabla_h\phi_{i,j} = (D_x\phi_{i+\frac{1}{2},j}, D_y\phi_{i,j+\frac{1}{2}}),$$

and the discrete divergence $\nabla_h\cdot : \vec{\mathcal{E}}_{m\times n} \to C_{m\times n}$ becomes

$$\nabla_h \cdot f_{i,j} = d_x f^x_{i,j} + d_y f^y_{i,j}, \quad \text{for } f = (f^x, f^y) \in \vec{\mathcal{E}}_{m\times n}. \tag{3.1}$$

The standard 2D discrete Laplacian Δ_h, which maps from $C_{\tilde{m}\times\tilde{n}}$ to $C_{m\times n}$, is defined as follows:

$$\begin{aligned} \Delta_h\phi_{i,j} &= d_x\left(D_x\phi\right)_{i,j} + d_y\left(D_y\phi\right)_{i,j}\\ &= \tfrac{1}{h_x^2}\left(\phi_{i+1,j} + \phi_{i-1,j} - 2\phi_{i,j}\right) + \tfrac{1}{h_y^2}\left(\phi_{i,j+1} + \phi_{i,j-1} - 2\phi_{i,j}\right). \end{aligned} \tag{3.2}$$

To provide a clearer visualization, the spatial arrangement of the cell-centered and edge-centered points is schematically presented in Fig. 2. In the summarized framework of spatial discretization, the grid points are divided into three types: cell-centered points, edge-centered points, and ghost points. The cell-centered and edge-centered points correspond to the locations where scalar and vector fields are defined, respectively, while the ghost points are virtual points used for boundary treatment, facilitating the computation of difference operators at the boundaries.

The differential operators follow distinct mapping paths:

- Gradient operator ∇_h: **Cell-centered → Edge points**, (via D_x, D_y)
- Divergence operator $\nabla_h\cdot$: **Edge points → Cell-centered**, (via d_x, d_y)
- Consequently, the Laplace operator Δ_h follows the path:

$$\text{Cell-centered} \xrightarrow{\nabla_h} \text{Edge points} \xrightarrow{\nabla_h\cdot} \text{Cell-centered}$$

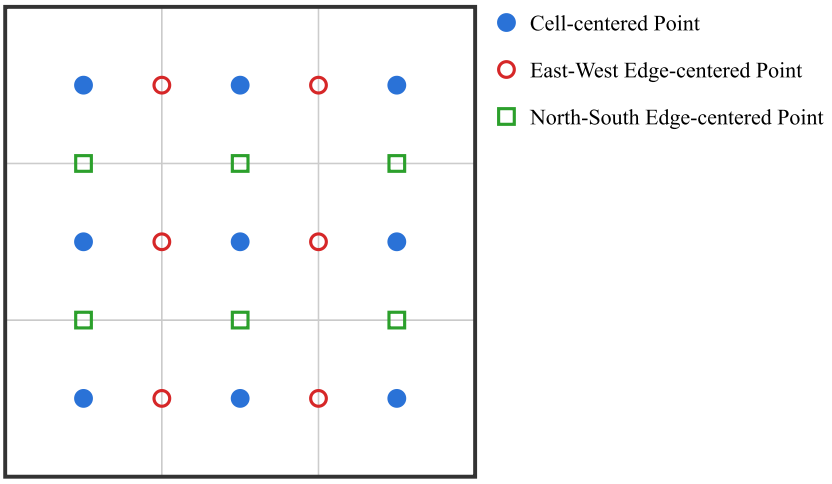

Fig. 2. The cell-centered finite difference grid.

In particular, all the physical variables in the PDE system, including ϕ_T, ϕ_N, ϕ_σ, ϕ_M and θ, are evaluated at the cell-centered grid point $(-1+(i-\frac{1}{2})h_x, -1+(j-\frac{1}{2})h_y)$, instead of the standard spatial coordinate point $(-1+ih_x, -1+jh_y)$. The key advantage of the cell-centered grid point over the standard spatial coordinate point is associated with the fact that, if a discrete inner product and discrete L^2 norm is taken into consideration, the integration weight values will be uniformly 1 for all the cell-centered grid points. Based on the fact that the cell-centered grid corresponds to the midpoint rule, where each grid point represents the center of an equal-sized cell, we see that all points have the same integration weight in the discrete integration. This would greatly simplify the theoretical analysis of convergence and error estimate, which will be carried out in subsequent work. In comparison, if the standard spatial coordinate point is used, the integration weight values will be retained as 1 at interior grid points, while such a weight value becomes $\frac{1}{2}$ on the boundary points to maintain the second order accuracy in the trapezoid summation formula. In turn, such a non-uniform distribution of the weight values in the discrete integration will make the theoretical analysis more complicated, although there is no essential difference in the mathematical principle; see the related theoretical works of the finite difference numerical schemes [34,36].

In the context of the problem of variable mobility, we also have the following discretization:

$$\mathrm{div}(M(\phi)\nabla_h\mu)_{i,j} = d_x\big(M\left(A_x\phi\right)D_x\mu\big)_{i,j} + d_y\big(M\left(A_y\phi\right)D_y\mu\big)_{i,j}. \tag{3.3}$$

For the numerical simulations, we assume that $m_x = n_y = N$, which implies $h_x = h_y = h$, where h represents the mesh size.

Remark 1. While we present the 2-D spatial discretization in this study, an extension to the 3-D case is straightforward. One can introduce a third spatial direction z and define corresponding cell-centered grids and edge-centered grids, as well as difference operators such as d_z, D_z, and A_z. Existing 3-D extensions have been provided in [34] for interested readers.

3.2. Fully discrete numerical scheme for ϕ_T

We introduce the stabilization constants, denoted as κ_{T_1} and κ_{T_2}.
Specifically, we have

$$\partial_t\phi_T + \mathcal{L}_{\kappa_T}\phi_T = N_T(\phi_T, \phi_V, \phi_\sigma, \theta), \tag{3.4}$$

$$\begin{aligned}
\mathcal{L}_{\kappa_T} &= -\kappa_{T_1}\Delta + \kappa_{T_2}\Delta^2,\\
N_T(\phi_T, \phi_V, \phi_\sigma, \theta) &= \nabla\cdot\left(m_T\left(\phi_V\right)\nabla\mu\right) - \nabla\cdot\left(\chi_H\phi_V\nabla\theta\right)\\
&\quad + \lambda_T^{\mathrm{pro}}\phi_\sigma\phi_V\left(1-\phi_T\right) - \lambda_T^{\mathrm{apo}}\phi_V - \kappa_{T_1}\Delta\phi_T + \kappa_{T_2}\Delta^2\phi_T,\\
\mu &= \bar{E}\left(4\phi_T^3 - 6\phi_T^2 + 2\phi_T\right) - \varepsilon_T^2\Delta\phi_T.
\end{aligned} \tag{3.5}$$

After the spatial semi-discretization of the Eq. (3.4) for ϕ_T using the central finite difference method discussed in Section 3.1, a system of ODEs is obtained:

$$\frac{d\Phi_T}{dt} + L_{\kappa_T,h}\Phi_T = N_T(\Phi_T, \Phi_V, \Phi_\sigma, \Theta), \tag{3.6}$$

where Φ_T is discretized as a vector over the grid points:

$$\Phi_T = \left(\phi_{T\,1,1}, \phi_{T\,1,2}, \ldots, \phi_{T\,1,N}, \phi_{T\,2,1}, \phi_{T\,2,2}, \ldots, \phi_{T\,2,N}, \ldots, \phi_{T\,N,1}, \ldots, \phi_{T\,N,N}\right)^T.$$

Similarly, Φ_σ, Φ_N, Φ_V, Θ are discretized in the same way as Φ_T:

$$\Phi_\sigma = \left(\phi_{\sigma 1,1}, \phi_{\sigma 1,2}, \dots, \phi_{\sigma N,N}\right)^T, \quad \Phi_N = \left(\phi_{N 1,1}, \phi_{N 1,2}, \dots, \phi_{N N,N}\right)^T,$$

$$\Phi_V = \left(\phi_{V 1,1}, \phi_{V 1,2}, \dots, \phi_{V N,N}\right)^T, \quad \Theta = \left(\theta_{1,1}, \theta_{1,2}, \dots, \theta_{N,N}\right)^T.$$

The terms Φ_T^3 and Φ_T^2 represent the cubic and quadratic terms of the discretized Φ_T, respectively:

$$\Phi_T^3 = \left(\phi_{T\,1,1}^{\,3}, \phi_{T\,1,2}^{\,3}, \dots, \phi_{T\,N,N}^{\,3}\right)^T, \quad \Phi_T^2 = \left(\phi_{T\,1,1}^{\,2}, \phi_{T\,1,2}^{\,2}, \dots, \phi_{T\,N,N}^{\,2}\right)^T.$$

$L_{\kappa_T,h}$ denotes the discrete matrix form associated with the spatially discretized operator $\mathcal{L}_{\kappa_T}$, and $N_T(\Phi_T, \Phi_V, \Phi_\sigma, \Theta)$ represents the spatially discretized nonlinear term.

Notice that, to balance the second-order and fourth-order terms in the Eq. (3.4) and to avoid high-frequency oscillations as well as numerical instability arising from the discretization process, we choose the stabilization parameters as $\kappa_{T_1} = 2M_T\bar{E}$ and $\kappa_{T_2} = (C\varepsilon_T)^2$, where C is a constant. Meanwhile, in the practical simulations, we set $C = 1/8$, since this constant would be sufficient to ensure numerical stability in extensive numerical experiments; also see the related analysis works of diffusion parameters for the Cahn-Hilliard type equations [36–39].

By using the integrating factor $\mathrm{e}^{-tL_{\kappa_T,h}}$ (or variation of constants formula [40]), we integrate the equation over a single time step from $t = t_n$ to $t = t_{n+1}$. The key idea of the variation of constants method is to represent the solution of a linear nonhomogeneous system as the summation of the homogeneous solution and an integral involving the nonhomogeneous term. For a general system $\frac{dy}{dt} + Ay = f(t)$, the exact solution is given by:

$$y(t) = \mathrm{e}^{-A(t-t_0)}y(t_0) + \int_{t_0}^{t} \mathrm{e}^{-A(t-s)}f(s)\,ds,$$

which serves as the foundation of exponential integrators.

By applying this idea to the semi-discrete system (3.6), we obtain the following integral form over a single time step:

$$\Phi_T\left(t_{n+1}\right) = \mathrm{e}^{-L_{\kappa_T,h}\tau}\Phi_T\left(t_n\right) + \int_0^\tau \mathrm{e}^{-L_{\kappa_T,h}(\tau-s)}N_T(\Phi_T(t_n+s), \Phi_V(t_n+s), \Phi_\sigma(t_n+s), \Theta(t_n+s))ds. \tag{3.7}$$

The ETD method builds on this integral representation by computing the contribution from the linear term exactly, while approximating the nonlinear term using interpolation in time. This strategy allows for enhanced stability and efficiency, especially when the stiffness is mainly due to the linear part.

The core idea behind the ETD method is to approximate the nonlinear part N_T of the integral in (3.7) using interpolation, while accurately evaluating the integral.

The fully discrete low-order ETD scheme comes from approximating $N_T(\Phi_T(t_n+s), \Phi_V(t_n+s), \Phi_\sigma(t_n+s), \Theta(t_n+s))$ with $N_T(\Phi_T(t_n), \Phi_V(t_n), \Phi_\sigma(t_n), \Theta(t_n))$. The detailed form is given by

$$\Phi_T^{n+1} = \mathrm{e}^{-L_{\kappa_T,h}\tau}\Phi_T^n + N_T(\Phi_T^n, \Phi_V^n, \Phi_\sigma^n, \Theta^n)\int_0^\tau \mathrm{e}^{-L_{\kappa_T,h}(\tau-s)}ds. \tag{3.8}$$

Alternatively, the fully discrete ETD Runge-Kutta method is derived by approximating $N_T(\Phi_T(t_n+s), \Phi_V(t_n+s), \Phi_\sigma(t_n+s), \Theta(t_n+s))$ with a linear interpolation based on $N_T(\Phi_T(t_n), \Phi_V(t_n), \Phi_\sigma(t_n), \Theta(t_n))$ and $N_T(\widetilde{\Phi}_T^{n+1}, \widetilde{\Phi}_V^{n+1}, \widetilde{\Phi}_\sigma^{n+1}, \Theta^n)$, and the form is represented as

$$\begin{cases} \widetilde{\Phi}_T^{n+1} = \mathrm{e}^{-L_{\kappa_T,h}\tau}\Phi_T^n + N_T(\Phi_T^n, \Phi_V^n, \Phi_\sigma^n, \Theta^n)\displaystyle\int_0^\tau \mathrm{e}^{-L_{\kappa_T,h}(\tau-s)}ds, \\ \Phi_T^{n+1} = \mathrm{e}^{-L_{\kappa_T,h}\tau}\Phi_T^n + \displaystyle\int_0^\tau \mathrm{e}^{-L_{\kappa_T,h}(\tau-s)}\Big((1-\frac{s}{\tau})N_T(\Phi_T^n, \Phi_V^n, \Phi_\sigma^n, \Theta^n) \\ \qquad\qquad + \frac{s}{\tau}N_T(\widetilde{\Phi}_T^{n+1}, \widetilde{\Phi}_V^{n+1}, \widetilde{\Phi}_\sigma^{n+1}, \Theta^n)\Big)ds. \end{cases} \tag{3.9}$$

The Φ_σ^n, $\widetilde{\Phi}_\sigma^{n+1}$, $\Phi_V^n = \Phi_T^n - \Phi_N^n$ and Θ^n will be described in Section 3.4.1, Section 3.3 and Section 3.6.

In biological modeling, the order parameter Φ_T should remain within the $[0, 1]$ range, to maintain the physical relevance. Therefore, we apply a cut-off operator to update Φ_T^{n+1} and $\widetilde{\Phi}_V^{n+1} = \mathscr{C}(\widetilde{\Phi}_T^{n+1}) - \Phi_N^n$. It is well known that the Cahn-Hilliard type evolutionary equation does not satisfy the maximum principle, since it is in the H^{-1} gradient flow structure. In fact, its solution may develop a maximum norm greater than 1 in finite time, as proved in an existing theoretical work [38]. Therefore, a cut-off process turns out to be a useful tool. In our future work, we plan to develop numerical methods that satisfy the MBP without relying on cut-off, in order to overcome this limitation. Therefore, an appearance of a numerical solution of Φ_T^{n+1} with a maximum norm greater than 1 does not come from the numerical instability; instead, such a numerical behavior is associated with the PDE analysis of this Cahn-Hilliard type equation. On the other hand, since the numerical values of $\widetilde{\Phi}_T^{n+1}$ usually stay within a slightly deviated range of order $[-O(\epsilon), 1 + O(\epsilon)]$ in most experiments, as demonstrated in the simulation of Cahn-Hilliard type equation, this approach ensures that the numerical solution meets physical properties and prevents non-physical values in simulations. This cut-off approach ensures that the numerical schemes for the remaining four variables automatically satisfy the MBP and preserve the bound.

3.3. Fully discrete numerical scheme for ϕ_N

After the spatial semi-discretization of the Eq. (2.5), a system of ODEs based on the discrete grid points is obtained:

$$\frac{d\Phi_N}{dt} = \lambda_{VN}\mathcal{H}(\sigma_{VN} - \Phi_\sigma) \odot \Phi_V, \tag{3.10}$$

where the symbol $\odot$ denotes the Hadamard (element-wise) product. The trapezoidal rule is used to construct the fully discrete scheme for Φ_N:

$$\Phi_N^{n+1} = \Phi_N^n + \frac{\tau}{2}\Big(\lambda_{VN}\mathcal{H}(\sigma_{VN} - \Phi_\sigma^n) \odot \big(\Phi_T^n - \Phi_N^n\big) + \lambda_{VN}\mathcal{H}(\sigma_{VN} - \widetilde{\Phi}_\sigma^{n+1}) \odot \big(\Phi_T^{n+1} - \Phi_N^{n+1}\big)\Big), \tag{3.11}$$

where Φ_σ^n and $\widetilde{\Phi}_\sigma^{n+1}$ will be described in Section 3.4.1.

Theorem 1 (Discrete bound preservation for Φ_N of the trapezoidal rule scheme). *If the initial values satisfy $0 \le \phi^0_{N_{i,j}} \le \phi^0_{T_{i,j}} \le 1$, then the trapezoidal rule scheme (3.11) maintains the discrete bound preservation. Specifically, for any time step $\tau \le \frac{2}{\lambda_{VN}}$ (which is readily satisfied), the numerical solution $\phi^n_{N_{i,j}}$ generated by the trapezoidal rule scheme ensures that, for all $n \ge 0$, we have $0 \le \phi^n_{N_{i,j}} \le \phi^n_{T_{i,j}} \le 1$ holds for any t_{n+1}.*

Proof. A simplification of Eq. (3.11) gives us an update rule for $\phi^{n+1}_{N_{i,j}}$:

$$\begin{aligned}(1 + \frac{\tau}{2}\lambda_{VN}\mathcal{H}(\sigma_{VN} - \widetilde{\phi}^{n+1}_{\sigma_{i,j}}))\phi^{n+1}_{N_{i,j}} &= (1 - \frac{\tau}{2}\lambda_{VN}\mathcal{H}(\sigma_{VN} - \phi^n_{\sigma_{i,j}}))\phi^n_{N_{i,j}} \\ &+ \frac{\tau}{2}\Big(\lambda_{VN}\mathcal{H}(\sigma_{VN} - \phi^n_{\sigma_{i,j}})\phi^n_{T_{i,j}} + \lambda_{VN}\mathcal{H}(\sigma_{VN} - \widetilde{\phi}^{n+1}_{\sigma_{i,j}})\phi^{n+1}_{T_{i,j}}\Big),\end{aligned} \tag{3.12}$$

in which $\phi^n_{N_{i,j}} = \phi_N(x_i, y_j, t_n)$.

Given that $\phi^n_{N_{i,j}}$, $\phi^n_{T_{i,j}}$, and $\phi^{n+1}_{T_{i,j}}$ lie in $[0,1]$, $\tau \le \frac{2}{\lambda_{VN}}$, and using the definition of the $\mathcal{H}$ function, along with the fact that λ_{VN}, $1 + \frac{\tau}{2}\lambda_{VN}\mathcal{H}(\sigma_{VN} - \widetilde{\phi}^{n+1}_{\sigma_{i,j}})$, and $1 - \frac{\tau}{2}\lambda_{VN}\mathcal{H}(\sigma_{VN} - \phi^n_{\sigma_{i,j}})$ are all positive, we conclude that both the right-hand side and the coefficient of the left-hand side are non-negative. Therefore, we have $\phi^{n+1}_{N_{i,j}} \ge 0$. Moreover, we have

$$\begin{aligned}&(1 + \frac{\tau}{2}\lambda_{VN}\mathcal{H}(\sigma_{VN} - \widetilde{\phi}^{n+1}_{\sigma_{i,j}}))\phi^{n+1}_{N_{i,j}} \\ &\le 1 - \frac{\tau}{2}\lambda_{VN}\mathcal{H}(\sigma_{VN} - \phi^n_{\sigma_{i,j}}) + \frac{\tau}{2}\Big(\lambda_{VN}\mathcal{H}(\sigma_{VN} - \phi^n_{\sigma_{i,j}}) + \lambda_{VN}\mathcal{H}(\sigma_{VN} - \widetilde{\phi}^{n+1}_{\sigma_{i,j}})\Big) \\ &= 1 + \frac{\tau}{2}\lambda_{VN}\mathcal{H}(\sigma_{VN} - \widetilde{\phi}^{n+1}_{\sigma_{i,j}}).\end{aligned} \tag{3.13}$$

From Eq. (3.13), we deduce that $\phi^{n+1}_{N_{i,j}} \le 1$. Thus, we conclude that: $0 \le \phi^{n+1}_{N_{i,j}} \le 1$.

To prove $\phi^{n+1}_{N_{i,j}} \le \phi^{n+1}_{T_{i,j}}$, subtract $\phi^{n+1}_{T_{i,j}}$ from both sides of the Eq. (3.11):

$$\begin{aligned}&\Big(1 + \frac{\tau}{2}\lambda_{VN}\mathcal{H}(\sigma_{VN} - \widetilde{\phi}^{n+1}_{\sigma_{i,j}})\Big)\Big(\phi^{n+1}_{N_{i,j}} - \phi^{n+1}_{T_{i,j}}\Big) \\ &= \Big(1 - \frac{\tau}{2}\lambda_{VN}\mathcal{H}(\sigma_{VN} - \phi^n_{\sigma_{i,j}})\Big)\phi^n_{N_{i,j}} + \frac{\tau}{2}\lambda_{VN}\mathcal{H}(\sigma_{VN} - \phi^n_{\sigma_{i,j}})\phi^n_{T_{i,j}} - \phi^{n+1}_{T_{i,j}}\end{aligned} \tag{3.14}$$

We employ a proof by contradiction. Assume that there exists t_{n+1} such that $\phi^{n+1}_{N_{i,j}} > \phi^{n+1}_{T_{i,j}}$. By the definition of the Heaviside function and the non-negativity of τ and λ_{VN}, the coefficient of $\phi^{n+1}_{N_{i,j}} - \phi^{n+1}_{T_{i,j}}$ on the left-hand side is always positive. Therefore, the left-hand side of (3.14) is positive. Meanwhile, since $\phi^n_{N_{i,j}}$, $\phi^n_{T_{i,j}}$, and $\phi^{n+1}_{T_{i,j}}$ are all within $[0,1]$, the minimum value of the right-hand side could be non-positive. This contradicts the fact that the left-hand side is positive. Therefore, the assumption $\phi^{n+1}_{N_{i,j}} > \phi^{n+1}_{T_{i,j}}$ has to be false. Therefore, $0 \le \phi^{n+1}_{N_{i,j}} \le \phi^{n+1}_{T_{i,j}} \le 1$ hold for any t_{n+1}. Furthermore, since $\phi^{n+1}_{V_{i,j}} = \phi^{n+1}_{T_{i,j}} - \phi^{n+1}_{N_{i,j}}$, we also have $\phi^{n+1}_{V_{i,j}} \in [0,1]$. This completes the proof. □

3.4. Fully discrete numerical scheme for ϕ_σ

The numerical design is based on the MBP framework for semi-linear elliptic equations, as established by Du et al. [27]. By adhering to a specific set of conditions, we are able to apply the existing analysis. This allows us to readily derive the MBP and bound preserving properties. To facilitate the application of this framework, we first adopt the affine transformation, $\zeta(\gamma) : \mathbb{R}^d \to \mathbb{R}^d$ $(d \le 3)$, defined by the following equation:

$$\zeta(\gamma) = \frac{1}{2}\gamma + \frac{1}{2}, \quad \gamma \in \mathbb{R}^d. \tag{3.15}$$

Given ϕ_σ, by setting $\psi_\sigma = \zeta^{-1}(\frac{1}{|\phi^0_\sigma|_{\max}}\phi_\sigma)$, we can obtain an equivalent new equation for ψ_σ:

$$\partial_t\psi_\sigma = \frac{M_\sigma}{\delta_\sigma}\Delta\psi_\sigma - \lambda_\sigma\phi_V(\psi_\sigma + 1). \tag{3.16}$$

In turn, this formulation transforms the problem of ensuring $\phi_\sigma \in [0, |\phi_\sigma^0|_{\max}]$ into the equivalent problem of ensuring $\psi_\sigma \in [-1, 1]$.

Let us introduce a stabilization constant $\kappa_\sigma > 0$. Then the equation takes the form

$$\begin{aligned} &\partial_t \psi_\sigma + \mathcal{L}_{\kappa_\sigma} \psi_\sigma = \mathcal{N}_\sigma \psi_\sigma, \\ &\mathcal{L}_{\kappa_\sigma} = -\frac{M_\sigma}{\delta_\sigma}\Delta + \kappa_\sigma \mathcal{I}, \\ &\mathcal{N}_\sigma \psi_\sigma = \kappa_\sigma \psi_\sigma + f_{0,\sigma}(\phi_V, \psi_\sigma), \\ &f_{0,\sigma}(\phi_V, \psi_\sigma) = -\lambda_\sigma \phi_V(\psi_\sigma + 1). \end{aligned} \tag{3.17}$$

where $\mathcal{I}$ is the identity mapping, with the initial and homogeneous Neumann boundary conditions:

$$\psi_\sigma(0) = \frac{2\phi_{\sigma,0}}{|\phi_\sigma^0|_{\max}} - 1, \text{ in } \Omega, \qquad \frac{\partial \psi_\sigma}{\partial \mathbf{n}} = 0, \text{ on } [0, T] \times \partial\Omega, \tag{3.18}$$

In addition, the stabilization constant κ_σ is selected as

$$\kappa_\sigma \geq \max_{|\xi| \leq 1} \left| \frac{\partial f_{0,\sigma}}{\partial \psi_\sigma}(\phi_V, \xi) \right| = \max_{|\xi| \leq 1} | -\lambda_\sigma \phi_V | = \lambda_\sigma, \tag{3.19}$$

where ξ denotes any value in the interval $[-1, 1]$.

For the nonlinear term $f_{0,\sigma}$, notice that $\phi_V = \mathscr{C}(\phi_T) - \phi_N$ is within the interval $[0, 1]$ and λ_σ is nonnegative. For any $\beta_\sigma \geq 1$, the following inequality holds:

$$f_{0,\sigma}(\phi_V, \beta_\sigma) = -\lambda_\sigma \phi_V(\beta_\sigma + 1) \leq 0 \leq f_{0,\sigma}(\phi_V, -\beta_\sigma) = -\lambda_\sigma \phi_V(-\beta_\sigma + 1). \tag{3.20}$$

Then we have the following result.

Lemma 1. *Under the requirement (3.19), when $\phi_V \in [0, 1]$ for any $\xi \in [-\beta_\sigma, \beta_\sigma]$, it holds that*

$$|\mathcal{N}_\sigma[\xi]| \leq \kappa_\sigma \beta_\sigma. \tag{3.21}$$

In this study, we set $\beta_\sigma = 1$.

3.4.1. The fully discrete scheme

Applying the central finite difference method to (3.17) yields a system of ODEs:

$$\frac{d\Psi_\sigma}{dt} + L_{\kappa_\sigma, h} \Psi_\sigma = N_\sigma(\Phi_V, \Psi_\sigma), \tag{3.22}$$

where $L_{\kappa_\sigma, h}$ represents the discrete matrix form of the spatially discretized operator $\mathcal{L}_{\kappa_\sigma}$, and $N_\sigma(\Phi_V, \Psi_\sigma)$ denotes the spatially discretized nonlinear term.

By employing the ETD schemes provided in Section 3.2, the fully discrete low-order ETD scheme is derived:

$$\Psi_\sigma^{n+1} = \mathrm{e}^{-L_{\kappa_\sigma, h}\tau} \Psi_\sigma^n + N_\sigma(\Phi_V^n, \Psi_\sigma^n) \int_0^\tau \mathrm{e}^{-L_{\kappa_\sigma, h}(\tau - s)} ds. \tag{3.23}$$

Moreover, the fully discrete ETD Runge-Kutta scheme takes the form of

$$\begin{cases} \widetilde{\Psi}_\sigma^{n+1} = \mathrm{e}^{-L_{\kappa_\sigma, h}\tau} \Psi_\sigma^n + N_\sigma(\Phi_V^n, \Psi_\sigma^n) \displaystyle\int_0^\tau \mathrm{e}^{-L_{\kappa_\sigma, h}(\tau - s)} ds, \\ \Psi_\sigma^{n+1} = \mathrm{e}^{-L_{\kappa_\sigma, h}\tau} \Psi_\sigma^n + \displaystyle\int_0^\tau \mathrm{e}^{-L_{\kappa_\sigma, h}(\tau - s)} \left(\left(1 - \frac{s}{\tau}\right) N_\sigma(\Phi_V^n, \Psi_\sigma^n) + \frac{s}{\tau} N_\sigma(\widetilde{\Phi}_V^{n+1}, \widetilde{\Psi}_\sigma^{n+1}) \right) ds. \end{cases} \tag{3.24}$$

Hence, the numerical solutions of Eq. (2.7) can be deduced from the subsequent relationships:

$$\widetilde{\Phi}_\sigma^{n+1} = |\Phi_\sigma^0|_{\max} \frac{\widetilde{\Psi}_\sigma^{n+1} + 1}{2}, \quad \Phi_\sigma^n = |\Phi_\sigma^0|_{\max} \frac{\Psi_\sigma^n + 1}{2}, \tag{3.25}$$

3.4.2. Discrete MBP for ψ_σ

In order to prove the discrete MBP property, we need the following lemma.

Lemma 2 ([27]). *The Laplacian operator Δ generates a contraction semigroup $\{\mathrm{e}^{t\Delta}\}_{t \geq 0}$ on $C(\bar{\Omega})$, where $\bar{\Omega} = \Omega \cup \partial\Omega$, and the functions u in $C(\bar{\Omega})$ are continuous on the closed domain and satisfy the homogeneous Neumann boundary condition. For any $\alpha \geq 0$, it holds that*

$$\left\| \mathrm{e}^{t(\Delta - \alpha)} u \right\| \leq \mathrm{e}^{-\alpha t} \|u\|, \quad t \geq 0,$$

As indicated in [27], the spatially discrete approximation to the Laplacian Δ, namely Δ_h, satisfies Lemma 2. Specifically, the discrete Laplacian operator Δ_h, constructed by the standard central difference approximation under homogeneous Neumann boundary condition, leads to a symmetric and negative semi-definite matrix. Moreover, it satisfies the discrete maximum principle. As a result, the matrix exponential $\{\mathrm{e}^{t\Delta_h}\}_{t \geq 0}$ forms a contraction semigroup. Therefore, Δ_h satisfies the conditions in Lemma 2. Thus, based on Lemma 2, we can obtain the following discrete MBP theorem.

Theorem 2 (Discrete MBP for Ψ_σ of ETD schemes). *If $\|\psi_\sigma(\cdot,t_0)\|_\infty \le 1$ and κ_σ satisfies (3.19), then the ETD scheme (3.23) and the ETDRK scheme (3.24) unconditionally preserve the discrete MBP. In other words, for any time step size $\tau > 0$, the solutions satisfy: $\|\Psi_\sigma^n\|_\infty \le 1$, for any $n \ge 0$.*

Proof. Since $\|\psi_\sigma(\cdot,t_0)\|_\infty \le 1$, it suffices to prove the theorem for the case $\|\Psi_\sigma^n\|_\infty \le 1$ and then deduce $\|\Psi_\sigma^{n+1}\|_\infty \le 1$ for any n.

For the ETD scheme (3.23), an application of Lemmas 1 and 2, as well as the fact that $\|\Psi_\sigma^n\|_\infty \le 1$, implies that

$$\begin{aligned}\|\Psi_\sigma^{n+1}\|_\infty &\le \|e^{-L_{\kappa_\sigma,h}\tau}\|_\infty \|\Psi_\sigma^n\|_\infty + \int_0^\tau \|e^{-L_{\kappa_\sigma,h}(\tau-s)}\|_\infty \|N_\sigma(\Phi_V^n,\Psi_\sigma^n)\|_\infty ds,\\ &\le e^{-\kappa_\sigma\tau} + \int_0^\tau e^{-\kappa_\sigma(\tau-s)}\kappa_\sigma ds = e^{-\kappa_\sigma\tau} + \frac{1-e^{-\kappa_\sigma\tau}}{\kappa_\sigma}\kappa_\sigma = 1.\end{aligned} \tag{3.26}$$

Similarly, for the ETDRK scheme (3.24), an application of the two lemmas, combined with the inequalities that $\|\Psi_\sigma^n\|_\infty \le 1$, $\|\widetilde{\Psi}_\sigma^{n+1}\|_\infty \le 1$ (based on (3.26)), gives

$$\begin{aligned}\left\|\Psi_\sigma^{n+1}\right\|_\infty &\le \left\|e^{-L_{\kappa_\sigma,h}\tau}\right\|_\infty \left\|\Psi_\sigma^n\right\|_\infty\\ &\quad + \int_0^\tau \|e^{-L_{\kappa_\sigma,h}(\tau-s)}\|_\infty \left\|(1-\tfrac{s}{\tau})N_\sigma(\Phi_V^n,\Psi_\sigma^n) + \tfrac{s}{\tau}N_\sigma(\widetilde{\Phi}_V^{n+1},\widetilde{\Psi}_\sigma^{n+1})\right\|_\infty ds,\\ &\le e^{-\kappa_\sigma\tau} + \int_0^\tau e^{-\kappa_\sigma(\tau-s)}\left((1-\tfrac{s}{\tau})\kappa_\sigma + \tfrac{s}{\tau}\kappa_\sigma\right)ds,\\ &= e^{-\kappa_\sigma\tau} + \frac{1-e^{-\kappa_\sigma\tau}}{\kappa_\sigma}\kappa_\sigma = 1.\end{aligned}$$

This completes the proof. □

According to (3.25) and (3.19), it is obvious that if $\phi_\sigma(\cdot,t_0) \in [0, |\phi_\sigma^0|_{\max}]$ (or equivalently $\|\psi_\sigma(\cdot,t_0)\|_\infty \le 1$), then the numerical solution satisfies $\phi_\sigma(\cdot,t) \in [0, |\phi_\sigma^0|_{\max}]$ for all $t > 0$.

Remark 2. Notice that the introduction of the stabilization constant κ_σ is to ensure the validity of the MBP. When κ_σ satisfies the conditions in Theorem 2, the MBP guarantees the boundedness of the numerical solution. As a measure of numerical stability, the MBP ensures that the solution does not blow up during the computation, which is particularly important when large time steps and large-scale computations are used.

The parameters κ_σ and β_σ are artificial stabilization factors introduced to ensure the boundedness of the nonlinear term and the stability of the numerical scheme. As shown in Lemma 1, both parameters are chosen to satisfy the theoretical conditions given in inequalities (3.19) and (3.20). In particular, inequality (3.20) requires $\beta_\sigma \ge 1$. To minimize the influence of artificial stabilization and reduce the amplitude of the stabilization terms, we set $\beta_\sigma = 1$ in this study, which is sufficient in the practical computations; also see the related analysis of artificial regularization parameters for various gradient flow equations [36,39,41,42].

3.5. Fully discrete numerical scheme for ϕ_M

Similar to the nutrient concentration equation outlined in Section 3.4, by setting $\psi_M = \zeta^{-1}(\phi_M)$, in which ϕ_M is the volume fraction of MDE, we obtain an equivalent equation for ψ_M:

$$\partial_t\psi_M = M_M\Delta\psi_M - \lambda_M^{\mathrm{dec}}(\psi_M+1) + \lambda_M^{\mathrm{pro}}\phi_V\theta\frac{\sigma_H}{\sigma_H+\phi_\sigma}(1-\psi_M) - \lambda_\theta^{\mathrm{dec}}\theta(\psi_M+1). \tag{3.27}$$

This transforms the problem of ensuring $\phi_M \in [0,1]$ into an equivalent problem of ensuring $\psi_M \in [-1,1]$.

An introduction of a stabilization constant $\kappa_M > 0$ gives

$$\partial_t\psi_M + \mathcal{L}_{\kappa_M}\psi_M = \mathcal{N}_M\psi_M, \tag{3.28}$$

where

$$\begin{aligned}&\mathcal{L}_{\kappa_M} = -M_M\Delta + \kappa_M\mathcal{I}, \quad \mathcal{I}\ \mathrm{is\ the\ identity\ mapping},\\ &\mathcal{N}_M\psi_M = \kappa_M\psi_M + f_{0,M}(\phi_V,\psi_M,\phi_\sigma,\theta),\\ &f_{0,M}(\phi_V,\psi_M,\phi_\sigma,\theta) = -\lambda_M^{\mathrm{dec}}(\psi_M+1) + \lambda_M^{\mathrm{pro}}\phi_V\theta\frac{\sigma_H}{\sigma_H+\phi_\sigma}(1-\psi_M) - \lambda_\theta^{\mathrm{dec}}\theta(\psi_M+1).\end{aligned} \tag{3.29}$$

with the initial and homogeneous Neumann boundary conditions:

$$\psi_M(0) = 2\phi_{M,0} - 1, \ \text{in } \Omega, \qquad \frac{\partial\psi_M}{\partial\mathbf{n}} = 0, \ \text{on } [0,T]\times\partial\Omega, \tag{3.30}$$

The stabilization constant κ_M should be chosen as follows:

$$\begin{aligned}\kappa_M \ge \max_{|\xi|\le1}\left|\frac{\partial f_{0,M}(\phi_V,\psi_M,\phi_\sigma,\theta)}{\partial\psi_M}(\phi_V,\xi,\phi_\sigma,\theta)\right| &= \max_{|\xi|\le1}|-\lambda_M^{\mathrm{dec}} - \lambda_M^{\mathrm{pro}}\phi_V\theta\frac{\sigma_H}{\sigma_H+\phi_\sigma} - \lambda_\theta^{\mathrm{dec}}\theta|\\ &= \lambda_M^{\mathrm{dec}} + \lambda_M^{\mathrm{pro}}|\theta|_{\max} + \lambda_\theta^{\mathrm{dec}}|\theta|_{\max}.\end{aligned} \tag{3.31}$$

The choice of κ_M and β_M is similar to that of κ_σ and β_σ, as described in Remark 2.

Regarding the nonlinear term $f_{0,M}$, it is noticed that if the initial condition $\theta_0 > 0$ and $\phi_M > 0$, then $\theta > 0$. A contradiction argument is applied to prove this fact. Suppose there exists t^* such that $\phi_M(t^*) > 0$ and $\theta(t^*) \le 0$. By the evolutionary Eq. (2.9), the derivative of θ is also greater than zero, i.e., θ is increasing. Therefore, we see that $\theta(t_0) \le \theta(t_1) \le \ldots \le \theta(t^*) \le 0$, which contradicts the fact that $\theta_0 \in [0,1]$. Hence, the assumption becomes invalid, so that $\theta > 0$ whenever $\phi_M > 0$. Given $\phi_V, \phi_\sigma \in [0,1]$, the parameters λ_M^{dec}, λ_M^{pro}, σ_H, and $\lambda_\theta^{\text{dec}}$ are all non-negative. As a result, for any β_M such that $\beta_M \ge 1$, the following inequality holds:

$$f_{0,M}(\phi_V, \beta_M, \phi_\sigma, \theta) \le 0 \le f_{0,M}(\phi_V, -\beta_M, \phi_\sigma, \theta). \tag{3.32}$$

Then we have the following lemma.

Lemma 3. *Under the requirement (3.31), for any $\xi \in [-\beta_M, \beta_M]$, if ϕ_V, $\phi_\sigma \in [0,1]$, it holds that*

$$|\mathcal{N}_M[\xi]| \le \kappa_M \beta_M. \tag{3.33}$$

In this study, we set $\beta_M = 1$.

3.5.1. Fully discrete scheme

Applying the central finite difference scheme in space to (3.28) results in the following system of ODEs:

$$\frac{d\Psi_M}{dt} + L_{\kappa_M,h}\Psi_M = N_M(\Phi_V, \Psi_M, \Phi_\sigma, \Theta), \tag{3.34}$$

where $\Psi_M = \left(\psi_{M\,1,1}, \psi_{M\,1,2}, \ldots, \psi_{M\,N,N}\right)^T$. Here, $L_{\kappa_M,h}$ denotes the discrete matrix form associated with the spatially discretized operator $\mathcal{L}_{\kappa_M}$, and $N_M(\Phi_V, \Psi_M, \Phi_\sigma, \Theta)$ represents the spatially discretized nonlinear term.

Then the fully discrete low-order ETD scheme is obtained:

$$\Psi_M^{n+1} = \mathrm{e}^{-L_{\kappa_M,h}\tau}\Psi_M^n + N_M(\Phi_V^n, \Psi_M^n, \Phi_\sigma^n, \Theta^n)\int_0^\tau \mathrm{e}^{-L_{\kappa_M,h}(\tau-s)}ds. \tag{3.35}$$

And the fully discrete ETD Runge-Kutta scheme is:

$$\begin{cases} \widetilde{\Psi}_M^{n+1} = \mathrm{e}^{-L_{\kappa_M,h}\tau}\Psi_M^n + N_M(\Phi_V^n, \Psi_M^n, \Phi_\sigma^n, \Theta^n)\displaystyle\int_0^\tau \mathrm{e}^{-L_{\kappa_M,h}(\tau-s)}ds, \\ \Psi_M^{n+1} = \mathrm{e}^{-L_{\kappa_M,h}\tau}\Psi_M^n + \displaystyle\int_0^\tau \mathrm{e}^{-L_{\kappa_M,h}(\tau-s)}\Big((1-\frac{s}{\tau})N_M(\Phi_V^n, \Psi_M^n, \Phi_\sigma^n, \Theta^n) \\ \qquad\qquad + \frac{s}{\tau}N_M(\widetilde{\Phi}_V^{n+1}, \widetilde{\Psi}_M^{n+1}, \widetilde{\Phi}_\sigma^{n+1}, \Theta^n)\Big)ds, \end{cases} \tag{3.36}$$

Therefore, the numerical solution to the Eq. (2.8) could be derived from the following relationships:

$$\widetilde{\Phi}_M^{n+1} = \frac{\widetilde{\Psi}_M^{n+1}+1}{2}, \quad \Phi_M^n = \frac{\Psi_M^n+1}{2}, \tag{3.37}$$

3.5.2. Discrete MBP for ψ_M

Theorem 3 (Discrete MBP for ψ_M of the ETD schemes)**.** *If $\|\psi_M(\cdot,t_0)\|_\infty \le 1$ and κ_M satisfies (3.31), then both the ETD scheme (3.35) and the ETDRK scheme (3.36) unconditionally preserve the discrete MBP. Specifically, for any time step $\tau > 0$, the solution to the ETD scheme (3.35) and the ETDRK scheme (3.36) satisfy $\|\Psi_M^n\|_\infty \le 1$ for all $n \ge 0$.*

Proof. Analogous to the proof of Theorem 2, we merely need to demonstrate that if $\|\Psi_M^n\|_\infty \le 1$, it can be inferred that $\|\Psi_M^{n+1}\|_\infty \le 1$ for any n.

For the ETD scheme (3.35), an application of Lemmas 2 and 3, combined with the fact that ${\phi_V}_{i,j}^n \in [0,1]$ and $\|\Psi_M^n\|_\infty \le 1$, indicates that

$$\begin{aligned} \|\Psi_M^{n+1}\|_\infty &\le \|\mathrm{e}^{-L_{\kappa_M,h}\tau}\|_\infty\|\Psi_M^n\|_\infty + \int_0^\tau \|\mathrm{e}^{-L_{\kappa_M,h}(\tau-s)}\|_\infty\|N_M(\Phi_V^n, \Psi_M^n, \Phi_\sigma^n, \Theta^n)\|_\infty ds, \\ &\le \mathrm{e}^{-\kappa_M\tau} + \int_0^\tau \mathrm{e}^{-\kappa_M(\tau-s)}\kappa_M ds = \mathrm{e}^{-\kappa_M\tau} + \frac{1-\mathrm{e}^{-\kappa_M\tau}}{\kappa_M}\kappa_M = 1. \end{aligned} \tag{3.38}$$

For the ETDRK scheme (3.36), since $\|\Psi_M^n\|_\infty \le 1$, and $\|\widetilde{\Psi}_M^{n+1}\|_\infty \le 1$ (based on (3.38)), we have

$$\begin{aligned} \|\Psi_M^{n+1}\|_\infty \le& \|\mathrm{e}^{-L_{\kappa_M,h}\tau}\|_\infty \cdot \|\Psi_M^n\|_\infty + \int_0^\tau \|\mathrm{e}^{-L_{\kappa_M,h}(\tau-s)}\|_\infty \\ &\cdot \left\|(1-\frac{s}{\tau})N_M(\Phi_V^n, \Psi_M^n, \Phi_\sigma^n, \Theta^n) + \frac{s}{\tau}N_M(\widetilde{\Phi}_V^{n+1}, \widetilde{\Psi}_M^{n+1}, \widetilde{\Phi}_\sigma^{n+1}, \Theta^n)\right\|_\infty ds, \\ \le& \mathrm{e}^{-\kappa_M\tau} + \int_0^\tau \mathrm{e}^{-\kappa_M(\tau-s)}\Big((1-\frac{s}{\tau})\kappa_M + \frac{s}{\tau}\kappa_M\Big)ds, \\ =& \mathrm{e}^{-\kappa_M\tau} + \frac{1-\mathrm{e}^{-\kappa_M\tau}}{\kappa_M}\kappa_M = 1. \end{aligned} \tag{3.39}$$

This completes the proof. □

Due to the relationships defined in (3.37), it is obvious that if $\phi_M(\cdot,t_0) \in [0,1]$ (or $\|\psi_M(\cdot,t_0)\|_\infty \le 1$), then it follows that $\phi_M(\cdot,t) \in [0,1]$ for all t.

3.6. Fully discrete numerical scheme for θ

Applying the central finite difference scheme in space to (2.9), resulting in the following system of ODEs:

$$\frac{d\Theta}{dt} = -\lambda_\theta^{\deg}\Theta \odot \Phi_M, \tag{3.40}$$

To discretize this equation, we adopt the trapezoidal rule, yielding the following numerical scheme:

$$\Theta^{n+1} = \Theta^n + \frac{\tau}{2}\left(-\lambda_\theta^{\deg}\Phi_M^n \odot \Theta^n - \lambda_\theta^{\deg}\Phi_M^{n+1} \odot \Theta^{n+1}\right). \tag{3.41}$$

Theorem 4 (Discrete bound preservation for θ of the Trapezoidal rule scheme)**.** *If $\theta_{i,j}^0 \in [0, \theta_{\max}^0], \forall i, j$, then the trapezoidal rule scheme (3.41) preserves the discrete bound. That is, for any time step size $\tau \le \frac{2}{\lambda_\theta^{\deg}}$ (which is easy to satisfy), then the trapezoidal rule numerical solution satisfies: $\theta_{i,j}^n \in [0, \theta_{\max}^0], \forall i, j$, for any $n \ge 0$.*

Proof. If we can prove that if $\theta_{i,j}^n \in [0, \theta_{\max}^0]$, then $\theta_{i,j}^{n+1} \in [0, \theta_{\max}^0]$, the theorem will be proven. First, simplifying Eq. (3.41) yields the update formula for $\theta_{i,j}^{n+1}$:

$$\theta_{i,j}^{n+1} = \left(\frac{1 - \frac{\tau}{2}\lambda_\theta^{\deg}\phi_{M_{i,j}}^n}{1 + \frac{\tau}{2}\lambda_\theta^{\deg}\phi_{M_{i,j}}^{n+1}}\right)\theta_{i,j}^n, \quad \text{with } \theta_{i,j}^n = \theta(x_i, y_j, t_n). \tag{3.42}$$

where $\phi_{M_{i,j}}^n, \phi_{M_{i,j}}^{n+1} \in [0, 1]$ by Theorem 3, and $\lambda_\theta^{\deg} > 0$, we see that if $\tau \le \frac{2}{\lambda_\theta^{\deg}}$, then

$$0 \le \left(\frac{1 - \frac{\tau}{2}\lambda_\theta^{\deg}\phi_{M_{i,j}}^n}{1 + \frac{\tau}{2}\lambda_\theta^{\deg}\phi_{M_{i,j}}^{n+1}}\right) \le 1. \tag{3.43}$$

Combining this with the inductive hypothesis $\theta_{i,j}^n \in [0, \theta_{\max}^0]$, we obtain:

$$0 \le \theta_{i,j}^{n+1} \le \theta_{i,j}^n \le \ldots \le \theta_{\max}^0. \tag{3.44}$$

Here the parameter $\lambda_\theta^{\deg}$ is set to 1 in the practical computation, thus it is straightforward to make $\tau \le 2$ satisfied. The proof is complete. □

Remark 3. While the modeling framework and the ETDRK method used in this work are based on previous studies, our contribution lies in integrating ETD with the MBP within the context of this class of tumor growth phase-field models, resulting in numerical schemes that rigorously ensure the solution bound at the discrete level. These schemes are applicable to complex phase-field models of tumor growth. In contrast to the approach in [18], which employs cut-off functions to constrain all variables, our method provides a theoretical guarantee that the numerical solutions always remain within physically admissible bounds. In our numerical experiments, it is observed that the physical variables could exceed their physical range during the simulation without using a bound-preserving method, resulting in unphysical behavior and eventual failure of the computation. By contrast, our scheme consistently maintains physical feasibility throughout the simulation process, thereby significantly improving the stability and reliability of the algorithm.

3.7. Fast implementation of the ETD schemes

In the following, we provide an efficient implementation of the ETD schemes utilizing fast algorithms based on the Fast Fourier Transform (FFT).

The core computational bottleneck in the ETDRK schemes (3.9), (3.24), and (3.36) lies in the matrix exponential-vector products such as $e^{-L_{\kappa_T,h}\tau}$. To efficiently compute these terms, we first introduce the $\{\Upsilon_i\}_{i=0,1,2}$ functions constructed from e^{-L}. For large-scale problems, directly computing these products can be computationally expensive. In regular domains, the specific structure matrix allows the use of FFT-based fast algorithms, significantly improving computational efficiency.

The core idea behind FFT acceleration is to exploit orthogonal transformations to convert spatial domain problems into the frequency domain for computational simplification. The rationale for using the Discrete Cosine Transform (DCT) lies in its compatibility with Neumann boundary conditions. Under such conditions, the eigenfunctions of the continuous Laplacian are cosine functions, and the DCT offers a natural discrete analog. In particular, the DCT diagonalizes the discrete Laplacian with Neumann boundary conditions, which makes it a suitable and efficient choice for transforming the differential operator into a diagonal form. This makes the DCT an ideal tool for diagonalizing the operator. More specifically, the operator L can be diagonalized as $L = C^{-1}\Lambda C$, where C is the DCT transformation matrix and Λ is a diagonal matrix of eigenvalues. This allows the computation to proceed as follows: first, apply the DCT to transform the vector from physical space to frequency space; next, perform element-wise multiplication in the frequency domain; finally, apply the inverse DCT to transform the result back to the physical domain. Moreover, the DCT itself can be efficiently implemented using FFT: by appropriately extending the original data array and applying FFT, the necessary DCT coefficients can be extracted with reduced computational cost.

Before applying FFT-based acceleration, we first present the Algorithm 1 of the ETDRK scheme to facilitate the subsequent use of fast algorithms. We represent $\Phi_T^n, \Phi_N^n, \Phi_V^n, \Phi_\sigma^n, \Phi_M^n, \Theta^n \in \mathbb{R}^{N\times N}$ in matrix form with entries $\phi_{T\,i,j}^n$, $\phi_{N\,i,j}^n$ $\phi_{V\,i,j}^n$, $\phi_{\sigma\,i,j}^n$, $\phi_{M\,i,j}^n$, $\theta_{i,j}^n$, and

Algorithm 1 Fast implementation of the ETDRK scheme.

Input: Φ_T^n, Φ_V^n, Φ_σ^n, Ψ_σ^n, Ψ_M^n, Θ^n, Φ_N^n

Define:

$$\Upsilon_0(L) := e^{-L}, \quad \Upsilon_1(L) := \frac{1-e^{-L}}{L}, \quad \Upsilon_2(L) := \frac{e^{-L}-1+L}{L^2}$$

Step 1: Predictor calculation (Eqs. (3.9), (3.24) and (3.36))

$\widetilde{\Phi}_T^{n+1} \leftarrow \Upsilon_0(L_{\kappa_T,h}\tau)\Phi_T^n + \tau\Upsilon_1(L_{\kappa_T,h}\tau)N_T(\Phi_T^n, \Phi_V^n, \Phi_\sigma^n, \Theta^n)$

$\widetilde{\Psi}_\sigma^{n+1} \leftarrow \Upsilon_0(L_{\kappa_\sigma,h}\tau)\Psi_\sigma^n + \tau\Upsilon_1(L_{\kappa_\sigma,h}\tau)N_\sigma(\Phi_V^n, \Psi_\sigma^n)$

$\widetilde{\Psi}_M^{n+1} \leftarrow \Upsilon_0(L_{\kappa_M,h}\tau)\Psi_M^n + \tau\Upsilon_1(L_{\kappa_M,h}\tau)N_M(\Phi_V^n, \Psi_M^n, \Phi_\sigma^n, \Theta^n)$

Step 2: Mapping and cut-off update (intermediate variable computation, Eqs. (3.25),(2.14), and (2.13))

$\widetilde{\Phi}_\sigma^{n+1} \leftarrow |\Phi_\sigma^0|_{\max}(\widetilde{\Psi}_\sigma^{n+1}+1)/2$

$\widetilde{\Phi}_V^{n+1} \leftarrow \mathscr{C}(\widetilde{\Phi}_T^{n+1}) - \Phi_N^n$

$\hat{\Phi}_T^{n+1} \leftarrow \mathscr{C}(\widetilde{\Phi}_T^{n+1})$

Step 3: Second-stage correction (Eqs. (3.9), (3.24) and (3.36))

$\bar{\Phi}_T^{n+1} \leftarrow \hat{\Phi}_T^{n+1} + \tau\Upsilon_2(L_{\kappa_T,h}\tau)\big(N_T(\hat{\Phi}_T^{n+1}, \widetilde{\Phi}_V^{n+1}, \widetilde{\Phi}_\sigma^{n+1}, \Theta^n) - N_T(\Phi_T^n, \Phi_V^n, \Phi_\sigma^n, \Theta^n)\big)$

$\Psi_\sigma^{n+1} \leftarrow \widetilde{\Psi}_\sigma^{n+1} + \tau\Upsilon_2(L_{\kappa_\sigma,h}\tau)\big(N_\sigma(\widetilde{\Phi}_V^{n+1}, \widetilde{\Psi}_\sigma^{n+1}) - N_\sigma(\Phi_V^n, \Psi_\sigma^n)\big)$

$\Psi_M^{n+1} \leftarrow \widetilde{\Psi}_M^{n+1} + \tau\Upsilon_2(L_{\kappa_M,h}\tau)\big(N_M(\widetilde{\Phi}_V^{n+1}, \widetilde{\Psi}_M^{n+1}, \widetilde{\Phi}_\sigma^{n+1}, \Theta^n) - N_M(\Phi_V^n, \Psi_M^n, \Phi_\sigma^n, \Theta^n)\big)$

Step 4: Mapping and cut-off update (final solution update, Eqs. (3.25),(3.37), and (2.13))

$\Phi_\sigma^{n+1} \leftarrow |\Phi_\sigma^0|_{\max}(\Psi_\sigma^{n+1}+1)/2$

$\Phi_M^{n+1} \leftarrow (\Psi_M^{n+1}+1)/2$

$\Phi_T^{n+1} \leftarrow \mathscr{C}(\bar{\Phi}_T^{n+1})$

Output: $\Phi_T^{n+1}, \Phi_\sigma^{n+1}, \Phi_M^{n+1}$

define the operators

$$\mathcal{L}_{\kappa_T,h} = -\kappa_{T_1}\Delta_h + \kappa_{T_2}\Delta_h^2, \quad \mathcal{L}_{\kappa_\sigma,h} = -\frac{M_\sigma}{\delta_\sigma}\Delta_h + \kappa_\sigma \mathcal{I}, \quad \mathcal{L}_{\kappa_M,h} = -M_M\Delta_h + \kappa_M \mathcal{I}, \tag{3.45}$$

whose matrix forms are given by $L_{\kappa_T,h}$, $L_{\kappa_\sigma,h}$, and $L_{\kappa_M,h}$, respectively. Δ_h is the discrete Laplace operator with Neumann boundary conditions, using the central finite difference approximation as described in Section 3.1. The spectral structure of the resulting discrete Laplacian is known, with eigenvalue calculation detailed in [26,43].

Since (3.45) and the operators $\mathcal{L}_{\kappa_T,h}$, $\mathcal{L}_{\kappa_\sigma,h}$, and $\mathcal{L}_{\kappa_M,h}$ arise from the discretization of the operators $\mathcal{L}_{\kappa_T}$, $\mathcal{L}_{\kappa_\sigma}$, and $\mathcal{L}_{\kappa_M}$ with Neumann boundary conditions, these discrete operators are diagonalizable and have the following eigenvalue decompositions, as shown in [26,43]:

$$\mathcal{L}_{\kappa_T,h} := \mathcal{C}^{-1}\Lambda_T\mathcal{C}, \quad \mathcal{L}_{\kappa_\sigma,h} := \mathcal{C}^{-1}\Lambda_\sigma\mathcal{C}, \quad \mathcal{L}_{\kappa_M,h} := \mathcal{C}^{-1}\Lambda_M\mathcal{C}, \tag{3.46}$$

where $\mathcal{C}$ represents the 2D DCT operator, and $\mathcal{C}^{-1}$ is the 2D inverse Discrete Cosine Transform (iDCT). For any $V = (V_{k,l}) \in \mathbb{C}^{(N+1)\times(N+1)}$, the following holds for the eigenvalue operations:

$$\big(\Lambda_T V\big)_{k,l} = \lambda_{T,k,l}V_{k,l}, \quad \big(\Lambda_\sigma V\big)_{k,l} = \lambda_{\sigma,k,l}V_{k,l}, \quad \big(\Lambda_M V\big)_{k,l} = \lambda_{M,k,l}V_{k,l}, \quad 1 \le k,l \le N+1, \tag{3.47}$$

where $\lambda_{T,k,l}$, $\lambda_{\sigma,k,l}$, and $\lambda_{M,k,l}$ denote the eigenvalues of the operators $\mathcal{L}_{\kappa_T,h}$, $\mathcal{L}_{\kappa_\sigma,h}$, and $\mathcal{L}_{\kappa_M,h}$, respectively. These eigenvalues are computed as follows:

$$\begin{aligned}
\lambda_{T,k,l} &= -\kappa_{T_1}\big(d_k^x + d_l^y\big) + \kappa_{T_2}\big(d_k^x + d_l^y\big)^2, \quad k,l = 1,2,\dots,N+1,\\
\lambda_{\sigma,k,l} &= \kappa_\sigma - \frac{M_\sigma}{\delta_\sigma}\big(d_k^x + d_l^y\big), \quad k,l = 1,2,\dots,N+1,\\
\lambda_{M,k,l} &= \kappa_M - M_M\big(d_k^x + d_l^y\big), \quad k,l = 1,2,\dots,N+1,
\end{aligned} \tag{3.48}$$

where

$$d_k^x = -\frac{4}{h^2}\sin^2\left(\frac{(k-1)\pi}{2N}\right), \quad d_l^y = -\frac{4}{h^2}\sin^2\left(\frac{(l-1)\pi}{2N}\right), \quad k,l = 1,2,\dots,N+1. \tag{3.49}$$

By Lemma 2.2 (4) in [26], applying a function to the operator (e.g., e^{-L}) reduces to applying the function to its eigenvalues, enabling fast computation via DCT: $f(L) = \mathcal{C}^{-1}f(\Lambda)\mathcal{C}$.

According to Lemma 2.2 (4) in [26], for $i = 0,1,2$, the following holds:

$$\begin{aligned}
\Upsilon_i\Big(\mathcal{L}_{\kappa_T,h}\tau\Big) &= \mathcal{C}^{-1}\Upsilon_i(\Lambda_T\tau)\mathcal{C}, \quad \big(\Upsilon_i(\Lambda_T\tau)V\big)_{k,l} = \Upsilon_i\big(\lambda_{T,k,l}\tau\big)V_{k,l}, \quad k,l = 1,2,\dots,N+1,\\
\Upsilon_i\Big(\mathcal{L}_{\kappa_\sigma,h}\tau\Big) &= \mathcal{C}^{-1}\Upsilon_i(\Lambda_\sigma\tau)\mathcal{C}, \quad \big(\Upsilon_i(\Lambda_\sigma\tau)V\big)_{k,l} = \Upsilon_i\big(\lambda_{\sigma,k,l}\tau\big)V_{k,l}, \quad k,l = 1,2,\dots,N+1,\\
\Upsilon_i\Big(\mathcal{L}_{\kappa_M,h}\tau\Big) &= \mathcal{C}^{-1}\Upsilon_i(\Lambda_M\tau)\mathcal{C}, \quad \big(\Upsilon_i(\Lambda_M\tau)V\big)_{k,l} = \Upsilon_i\big(\lambda_{M,k,l}\tau\big)V_{k,l}, \quad k,l = 1,2,\dots,N+1.
\end{aligned} \tag{3.50}$$

This means transforming to frequency domain by DCT, multiplying elementwise by $f(\Lambda)$, then inverse DCT to return, efficiently performing matrix function-vector multiplication. Algorithm 2 describes a fast implementation of the DCT using the FFT in the

Algorithm 2 Fast DCT via 1D FFT (x-direction).

Require: Input vector $\phi = [\phi_1, \phi_2, \dots, \phi_{N+1}]^T$
Ensure: Approximate DCT coefficients
1: Let $N \leftarrow \text{length}(\phi) - 1$
2: Construct reflection vector:

$$\hat{\phi} \leftarrow [\phi_N, \phi_{N-1}, \dots, \phi_2]^T$$

3: Form combined vector:

$$v \leftarrow \text{concat}(\phi, \hat{\phi})$$

4: Compute $2N$-point FFT:

$$\tilde{v} \leftarrow \text{FFT}(v)$$

5: Extract first $N+1$ components:

$$\tilde{v}_{\text{trunc}} \leftarrow \tilde{v}[1 : N+1]$$

6: Compute DCT approximation:

$$\text{DCT}(\phi) \leftarrow \frac{1}{2} \cdot \tilde{v}_{\text{trunc}}$$

7: **return** DCT(ϕ)

x-direction. In the 2D case, we repeat the same steps along the y-direction. For further details, see Sec. 4.4– 4.5 in [43].

Thus, the overall computational complexity of the proposed schemes is reduced from $O(N^3)$ to $O(N^2 \log_2 N)$ per time step through FFT-based fast calculations in two dimensions.

4. Numerical simulations of tumor growth model with ECM degradation

This section presents the simulation results obtained using the previously introduced tumor growth model and the proposed numerical algorithm. Simulations are performed with different initial ECM conditions, and both the temporal and spatial convergence are verified to demonstrate the effectiveness of the numerical algorithm. In addition, we simulate the growth of both aggressive and baseline tumors, discuss the impact of nutrient supply, the effect of varying MDE expression levels on ECM degradation, and the influence of different haptotaxis parameters on tumor growth. Both 2D and 3D tumor growth models are considered, with parameter values specified in Table 1, including the total tumor, necrotic core, and viable tumor. Furthermore, the MBP and bound-preserving properties are tested.

4.1. Two-dimensional tumor growth simulations with ECM initial values surrounding the tumor tissue

First we focus on a 2D square domain $\Omega = (-1, 1)^2$. The initial condition for the total tumor volume fraction ϕ_T is given by a Gaussian function centered at the origin:

$$\phi_{T,0}(x, y) = \exp\left(1 - \frac{1}{1 - 16\left(x^2 + y^2\right)}\right). \tag{4.1}$$

Given that the volume fraction of the necrotic core is 0 at the initial time, the total tumor volume fraction is equivalent to the volume fraction of the viable tumor at the initial time. At the beginning of the simulation, the nutrient concentration is uniformly set to 1 throughout the domain, and the MDE volume fraction is initialized at 0. For the initial ECM value, we refer to Fig. 2 in reference [44], which illustrates that the ECM surrounds the tumor tissue, providing cellular support and forming a physical barrier. Then we set a similar initial condition for the ECM surrounding the tumor tissue. The initial ECM condition is defined by the following function:

$$\theta_0 = \frac{1}{2} + \frac{1}{2}\left(1 - 2\left|\phi_{T,0} - 0.5\right|\right), \tag{4.2}$$

This function provides a smooth transition from 1/2 to 1 at the edge of the ECM ring. It creates a smooth transition region near $\phi_{T,0} = 0.5$ (approximate tumor boundary), describing the characteristic pattern of ECM surrounding the tumor.

Notice that, for the nutrient consumption term, in reference [18] (Eq. (2.7)), the nutrient consumption term simplifies to $-\lambda_T^{\text{pro}} \phi_V$ after substituting the simulation parameters, which does not depend on the nutrient concentration ϕ_σ. We have chosen a concentration-dependent source term of the form $-\lambda_\sigma \phi_V \phi_\sigma$ in (2.7). When the nutrient concentration ϕ_σ is high, the nutrient

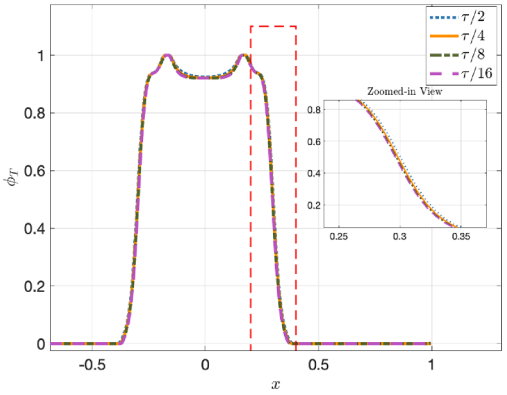

(a) Time convergence test of the solution ϕ_T along x at $y = 0$ and $t = 7$ for different time step sizes.

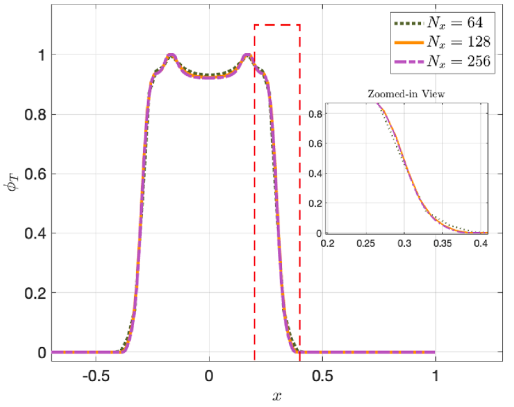

(b) Space convergence test of the solution ϕ_T along x at $y = 0$ and $t = 7$ for different spatial resolutions.

Fig. 3. Convergence test of the solution ϕ_T.

Table 2
Temporal convergence analysis for ϕ_T, ϕ_N and ϕ_σ with a fixed spatial grid of $N = 256$.

Time step	ϕ_T		ϕ_N		ϕ_σ	
	Error (L^∞)	Order	Error (L^∞)	Order	Error (L^∞)	Order
τ	3.55×10^{-2}	—	3.70×10^{-2}	—	6.49×10^{-3}	—
$\tau/2$	1.10×10^{-2}	1.69	1.07×10^{-2}	1.79	1.91×10^{-3}	1.76
$\tau/4$	3.14×10^{-3}	1.81	2.89×10^{-3}	1.89	5.41×10^{-4}	1.82
$\tau/8$	8.27×10^{-4}	1.92	7.62×10^{-4}	1.92	1.40×10^{-4}	1.95

Table 3
Temporal convergence analysis for ϕ_M and θ with a fixed spatial grid of $N = 256$.

Time step	ϕ_M		θ	
	Error (L^∞)	Order	Error (L^∞)	Order
τ	6.26×10^{-4}	—	1.28×10^{-3}	—
$\tau/2$	2.90×10^{-4}	1.11	5.79×10^{-4}	1.14
$\tau/4$	1.22×10^{-4}	1.25	2.38×10^{-4}	1.28
$\tau/8$	3.94×10^{-5}	1.63	7.86×10^{-5}	1.60

consumption by viable tumor cells increases; whereas, at lower concentrations, the consumption decreases. This concentration dependence allows the source term to reflect the changes in nutrient consumption by viable tumor cells at different nutrient levels, dynamically describing the process of nutrient consumption by viable tumor cells.

The temporal convergence test was conducted with a fixed spatial resolution of $m_x = n_y = N = 256$, $\tau = 4 \times 10^{-3}$, and time step sizes $\tau/2, \tau/4, \tau/8, \tau/16$ are considered. Fig. 3(a) displays the variation of ϕ_T in terms of x, at $y = 0$, $t = 7$. The convergence with different time step sizes is clearly observed. The detailed temporal convergence results for all five variables are presented in Tables 2 and 3. These results confirm that the numerical solution demonstrates a clear and stable convergence trend with time step refinement. Although the observed convergence order does not strictly reach second-order accuracy in time because of the cut-off operation used to enforce the bound-preserving property, this approach remains an effective strategy for ensuring both stability and physical admissibility of the numerical solutions. The spatial convergence test was performed with a fixed time step $\tau = 1 \times 10^{-4}$, and the spatial mesh is refined from $N = 64$ to $N = 256$. Fig. 3(b) shows the variation of ϕ_T in terms of x, at $y = 0$, $t = 7$, confirming the spatial convergence.

Based on the validated numerical schemes from the time and space convergence tests, we now discuss the results of tumor growth simulations with the boundary conditions given by (2.11) and the ECM initial conditions surrounding the tumor tissue.

The simulation runs up to a final time of $T = 10$. The time step size τ is chosen based on the boundedness conditions outlined in Theorems 1 and 4, which respectively require $\tau \le 2/\lambda_{VN}$ and $\tau \le 2/\lambda_\theta^{\deg}$. These conditions are satisfied with the parameter values provided in Table 1. Time convergence tests (see Fig. 3(a)) show that the numerical solution remains stable across different time step sizes. Therefore, we select $\tau = 1 \times 10^{-3}$ as an appropriate time step size for the subsequent simulations. In terms of spatial discretization, a uniform grid is employed with $m_x = n_y = N = 128$, ensuring adequate resolution to capture the dynamic evolution of

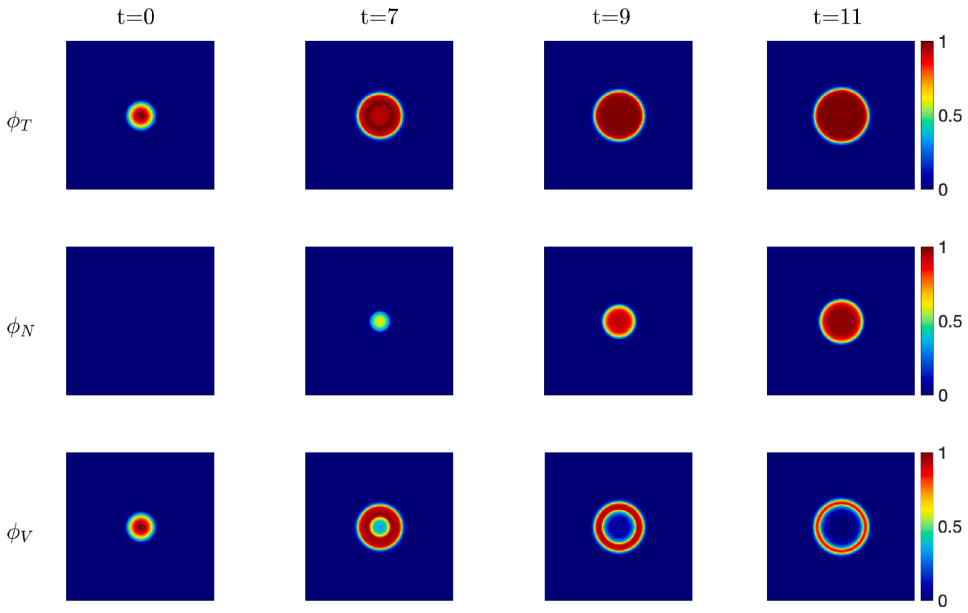

Fig. 4. The volume fraction evolution of total tumor cells ϕ_T, necrotic cells ϕ_N, and viable cells ϕ_V.

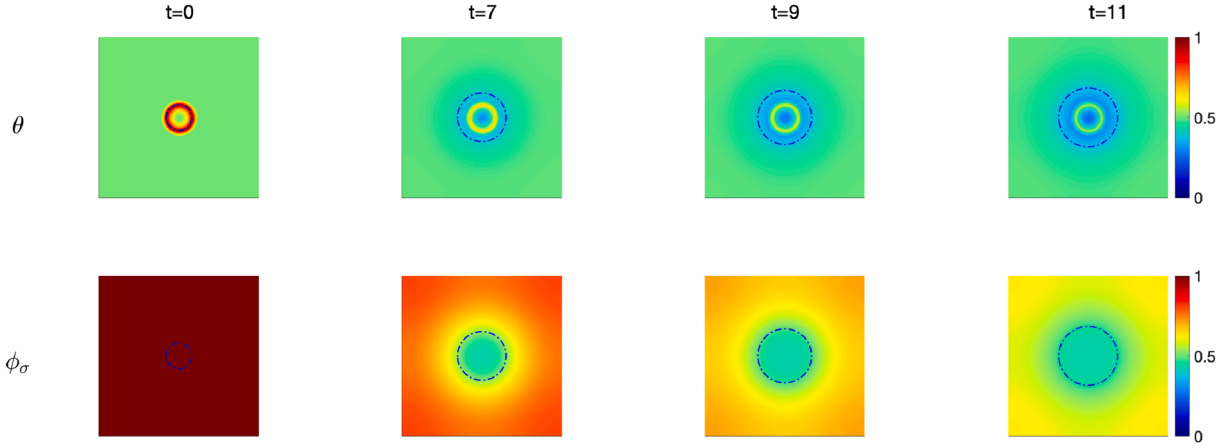

Fig. 5. Evolution of ECM density and nutrient concentration in the tumor growth.

the tumor interface. To guarantee the MBP for ψ_σ and ψ_M, the conditions from Theorems 2 and 3 should be satisfied, which results in the parameter choices $\kappa_\sigma \geq \lambda_\sigma$ and $\kappa_M \geq \lambda_M^{\mathrm{dec}} + \lambda_M^{\mathrm{pro}}|\theta|_{\max} + \lambda_\theta^{\mathrm{dec}}|\theta|_{\max}$.

Fig. 4 illustrates the simulated volume fractions of total tumor cells ϕ_T, necrotic cells ϕ_N, and viable cells ϕ_V at time instants $t = 0, 8, 9, 10$. Initially, at $t = 0$, there is no necrotic core. As time progresses, necrotic cells start to appear due to an insufficient supply of nutrients. The tumor forms a typical structure consisting of a "necrotic core" surrounded by an "active shell". Without the formation of new blood vessels (angiogenesis) to deliver extra oxygen and nutrients, the proportion of the necrotic core within the tumor will continue to increase over time.

In Fig. 5, the initial tumor is presented as a small circle, with the ECM distributed in a ring-like pattern around the tumor, forming a physical barrier. As the tumor grows, the MDEs released by viable tumor cells begin to degrade the ECM, which results in the degradation of the surrounding ECM of the tumor. While the tumor continuously consumes nutrients, leading to a decline in the nutrient concentration. The blue dashed line overlaid on the θ and ϕ_σ fields represents the approximate tumor boundary, defined by the $\phi_T \approx 0.5$ isoline. It is evident that the ECM and nutrient concentration are closely related to the tumor growth process, and their dynamic changes are crucial to the tumor microenvironment. Our simulations align well with the recent discoveries from [45]. Their study on primary tumor spheroids has demonstrated that the endogenous collagen matrix is "arranged predominantly around the 3D structure", forming a "capsule-like structure" similar to the initial ECM distribution in Fig. 5. Furthermore, they have observed an upregulation of matrix metalloproteinases (MMPs) in the 3D environment, and showed that enzymatic degradation of this matrix removes the physical barrier, which supports the ECM degradation dynamics modeled in our study.

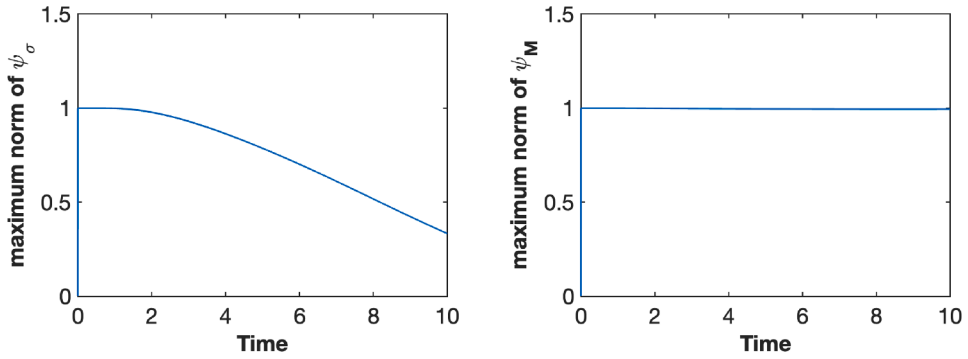

Fig. 6. MBP test of ψ_σ, and ψ_M.

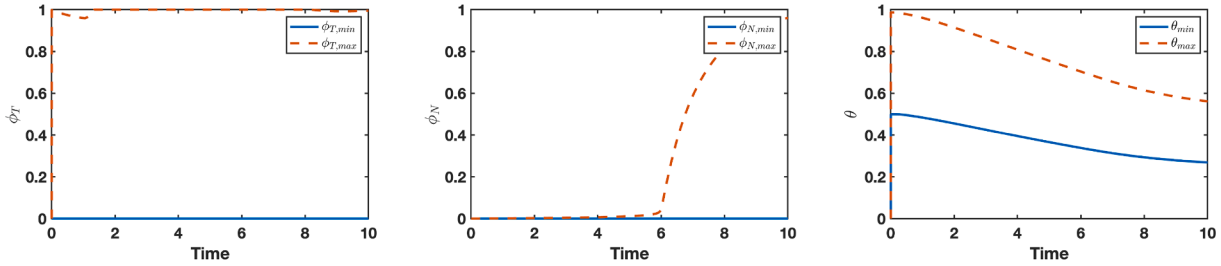

Fig. 7. Bound preserving test of ϕ_T, ϕ_N, and θ.

Table 4
Comparison of the ETDRK-MBP and improved Euler methods.

Method	Time Step	L^∞ Error	Status
ETDRK-MBP	$\tau/8$	2.326×10^{-4}	Stable
	$\tau/16$	6.963×10^{-5}	Stable
	$\tau/32$	1.986×10^{-5}	Stable
	$\tau/64$	5.176×10^{-6}	Stable
Improved Euler (with cut-off)	$\tau/8$	—	**Blow-up/Fails**
	$\tau/16$	2.624×10^{-1}	Stable
	$\tau/32$	8.838×10^{-2}	Stable
	$\tau/64$	2.836×10^{-2}	Stable
ETDRK (no MBP)	$\tau/8$	—	**Blow-up/Fails**
Improved Euler (no cut-off)	$\tau/8$	—	**Blow-up/Fails**

We have also performed the MBP test for ψ_σ and ψ_M, as well as the bound preserving test for ϕ_T, ϕ_N, and θ, as illustrated in Figs. 6 and 7. These tests have demonstrated that the numerical algorithm can effectively maintain the inherent properties of the model, which are crucial for accurately simulating tumor growth. This test further validates the effectiveness of our approach in handling complex biological processes.

Furthermore, we conducted a comparative analysis with the improved Euler method, a classical second-order scheme, as summarized in Table 4. Since the improved Euler method does not guarantee boundedness, a truncation (cut-off) was applied; otherwise, the simulation diverges rapidly. The numerical experiment was performed on a 256×256 grid up to a final time of $T = 2$. The base time step was set to $\tau = 4.0 \times 10^{-3}$, and the solution obtained with the finest step, $\tau/64$, was used as the reference for error calculation. The results demonstrate that at the large time step $\tau/8$, our ETDRK-MBP scheme remains stable, whereas the improved Euler method fails (or blows up) even with a cut-off mechanism applied. Moreover, even at its finest time step $\tau/64$ (error of 2.836×10^{-2}), the improved Euler method cannot achieve the accuracy attained by our ETDRK-MBP scheme at the much coarser time step $\tau/8$ (error of 2.326×10^{-4}). Therefore, our method achieves a favorable balance between accuracy and computational efficiency while allowing for relatively large time steps.

4.2. Two-dimensional tumor growth simulations with quasi-homogeneous ECM initial values

In the following simulations, we adopt the initial ECM setup from reference [18] to examine the interactions between the various biological factors under consideration.

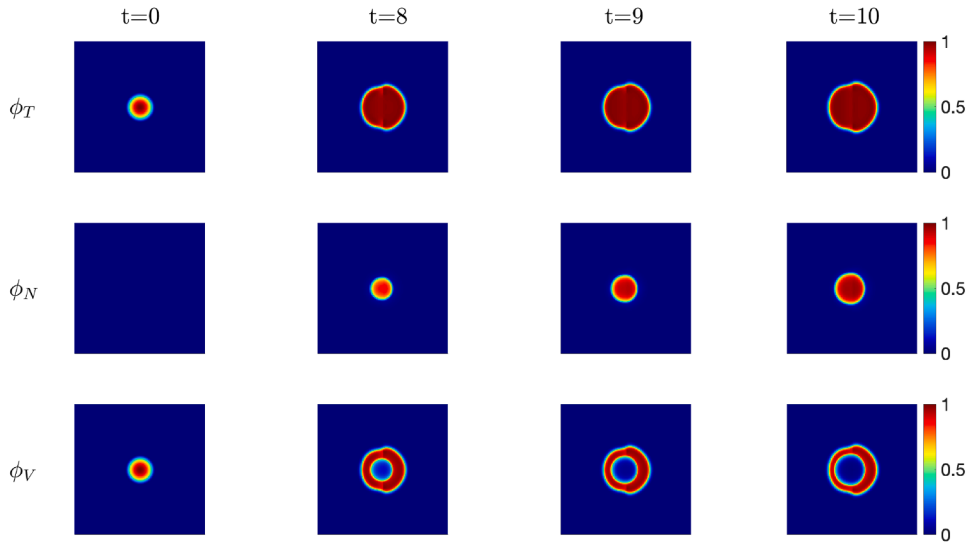

Fig. 8. The evolution of the volume fractions of total tumor cells ϕ_T , necrotic cells ϕ_N , and viable cells ϕ_V for the baseline tumor.

The initial conditions for ϕ_T, ϕ_N, and ϕ_M are set as in the previous section. At the beginning of the simulation, the nutrient concentration is uniformly set to 1 throughout the domain. Similar to the original study [18], a boundary condition of $\phi_\sigma = 1$ was imposed on the right side of the domain to simulate a constant nutrient source. Notice that the MBP for the diffusion operator remains valid under this mixed boundary conditions for ϕ_σ. Following the analysis in Section 2.4 of [27], if the global maximum occurs at an interior point or on a Neumann boundary, the inequality $\Delta\phi_\sigma \leq 0$ is satisfied. If the maximum occurs on the Dirichlet boundary, based on the fact that the boundary value is constrained to 1 (and the initial condition satisfies $\phi_\sigma^0 \leq 1$), it is clear that the diffusion operator still satisfies the conditions required for L^∞-dissipativity, thereby generating an L^∞-contraction semigroup. Consequently, the MBP remains valid. For such mixed boundary conditions, we numerically employed a fast algorithm strategy similar to that in Section 3.7. The fast DCT is applied in the direction with homogeneous Neumann boundary conditions (i.e., the y-direction), while a fast solver based on the modified Discrete Sine Transform-II is adopted in the direction with mixed boundary conditions (i.e., the x-direction). Further details on the fast algorithm for one-dimensional problems with mixed Neumann-Dirichlet boundary conditions could be found in Section 4.5.4 of [43]. The MDE volume fraction is initialized at 0, and the ECM density is divided into two regions: one half of the domain is set to 1, and the other half to 1/2.

The tumor simulated with the parameters in Table 1 is referred to as the baseline tumor. We first investigate the growth differences between the baseline tumor and aggressive tumors. Aggressive tumors may be represented by higher values of tumor proliferation and lower values of tumor apoptosis rate, for which the difference $|\lambda_T^{\text{pro}}| - |\lambda_T^{\text{apo}}|$ becomes larger (we chose $\lambda_T^{\text{pro}} = 2.5$ and $\lambda_T^{\text{apo}} = 0.001$ in simulations).

Fig. 8 illustrates the simulated volume fractions of total tumor cells ϕ_T, necrotic cells ϕ_N, and viable cells ϕ_V at time instants $t = 0, 8, 9, 10$ for the baseline tumor. Initially, as shown in the first column of Fig. 8, we begin with a small circular volume fraction of tumor cells without any necrotic regions. Over time, as the tumor grows and nutrients struggle to reach the center, a necrotic core gradually forms. Viable tumor cells arrange themselves into a ring-shaped structure. As time progresses, the necrotic core expands, and the viable tumor cells continue to proliferate. By the time instant $t = 10$, the tumor exhibits a necrotic core surrounded by viable tumor cells. Furthermore, it can be observed that the tumor moves toward the right side, where constant nutrients are provided, simulating a high-nutrient concentration environment. Fig. 9 illustrates the growth of aggressive tumors, which exhibit similar structural features. In contrast to the baseline tumor, the aggressive tumor shows an expansion in volume, an increase in the necrotic core size, and a thinning of the ring structure of viable cells.

In Fig. 10, the tumor continuously consumes the surrounding nutrients over time, reflecting the tumor's dependence on nutrient supply for growth. Meanwhile, compared to the baseline tumor, the aggressive tumor demonstrates faster nutrient depletion. Furthermore, Figs. 8–10 show that the tumor tends to expand into nutrient-rich areas to promote its growth and proliferation.

In the simulations, the aggressive tumor is modeled with a higher proliferation rate and a lower apoptosis rate, resulting in a rapid increase in the volume fraction of viable tumor cells (see Eq. (2.1)). According to the nutrient equation (see Eq. (2.7)), nutrient consumption is proportional to the volume fraction of viable tumor cells. Therefore, the aggressive tumor exhibits faster nutrient depletion. Furthermore, due to accelerated consumption and the lack of additional nutrient supply, nutrient-deficient regions are more likely to form within the tumor, leading to increased necrosis (higher ϕ_N). Fig. 12 presents cross-sectional profiles at y = 0 for both base and aggressive tumors at T = 10. The ϕ_T curve of the aggressive phenotype covers a wider spatial range and exhibits a higher peak value compared to the baseline tumor, quantitatively confirming its larger tumor size. This accelerated growth is directly quantified in Fig. 11. Despite being at the same time instant (T = 10), the aggressive phenotype (b) has already reached a larger size, with a tumor area and perimeter significantly greater than those of the baseline tumor (a) (Area: 0.54 vs. 0.40; Perimeter: 2.61 vs.

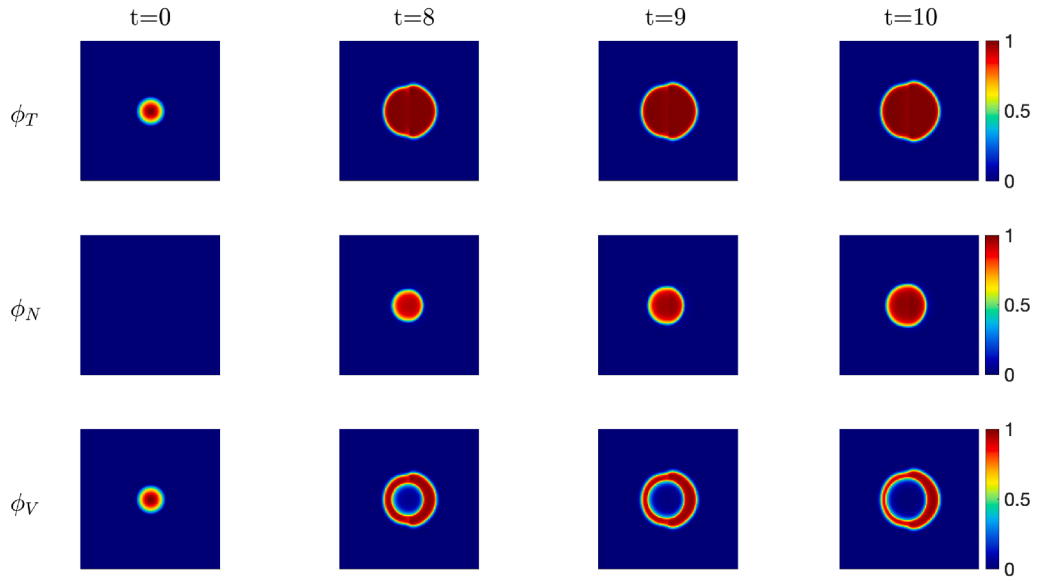

Fig. 9. The evolution of the volume fractions of total tumor cells ϕ_T , necrotic cells ϕ_N , and viable cells ϕ_V for the aggressive tumor.

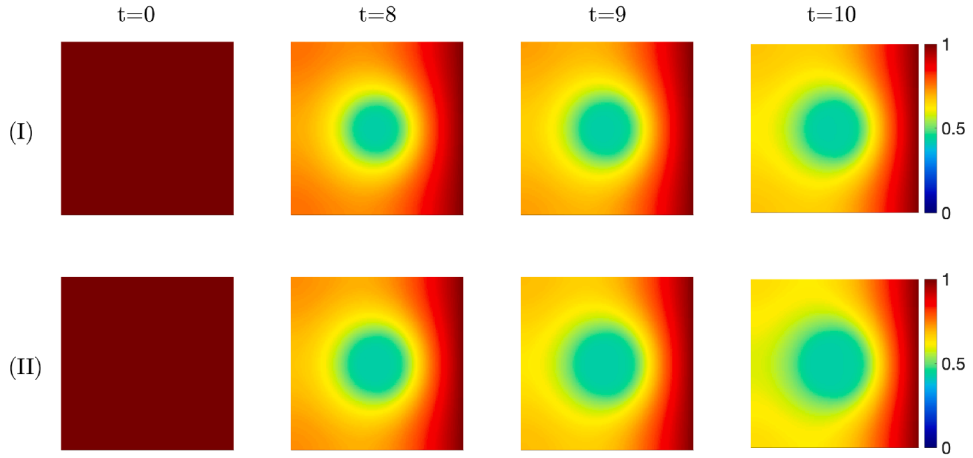

Fig. 10. Nutrient concentration distribution at $t = 0, 8, 9, 10$ for (I) baseline and (II)aggressive tumors.

2.25). These geometric measurements were obtained by analyzing the $\phi_T = 0.5$ contour, which defines the tumor boundary. The area was calculated using the polygonal area formula (Shoelace formula), while the perimeter was computed by summing the Euclidean distances between adjacent points along the contour. Furthermore, at a later stage (T = 30), the aggressive phenotype exhibits a more irregular tumor boundary contour compared to its earlier morphology, suggesting a trend towards invasive growth patterns, as visually demonstrated in Fig. 13.

Reference [18] presents simulation results of a mixed structure where necrotic and viable cells occupy approximately half of the central volume each ($\phi_N \approx \phi_V \approx 0.5$) over long-term estimation. In contrast, our simulation results indicate that the tumor undergoes stratification due to insufficient nutrient penetration as time progresses, ultimately forming a central necrotic core. As shown in Fig. (3c) of Hirschhaeuser et al. [46], the FaDu spheroid section exhibits “the typical architecture of a multicellular tumor spheroid with an outer viable rim and a necrotic core”. Egloff-Juras et al. [47] discovered that in FaDu spheroids, at day 3 the proliferative cells were present throughout the spheroid and by day 7, the necrotic core began to appear, “while the proliferative cells were mainly located on the periphery of the spheroid, which can be considered a typical spheroid morphology ”. Our simulation results have demonstrated behaviors similar to those described in these studies.

Next, we examine the effect of MDE expression on ECM degradation. In comparison with the baseline tumor, high MDE expression can be represented by higher MDE production rates and lower MDE decay rates, resulting in an increased difference $|\lambda_M^{\text{pro}}| - |\lambda_M^{\text{dec}}|$. Specifically, the parameters for high MDE expression are given by $\lambda_M^{\text{pro}} = 1.5$ and $\lambda_M^{\text{dec}} = 0.5$. In contrast, low MDE expression is

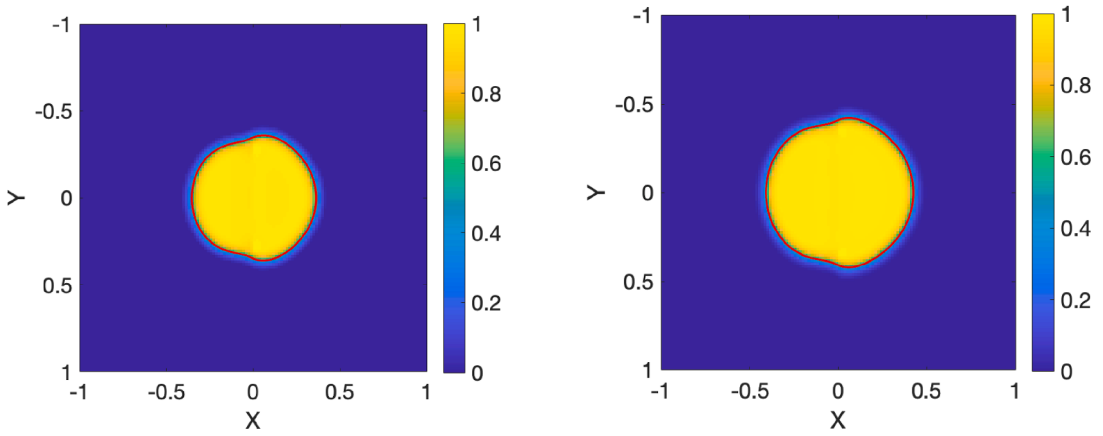

Fig. 11. Comparison of tumor growth at T = 10: (left) baseline tumor; (right) aggressive tumor. The red line indicates the tumor boundary, defined by the $\phi_T \approx 0.5$ isocontour. (For interpretation of the references to colour in this figure legend, the reader is referred to the web version of this article.)

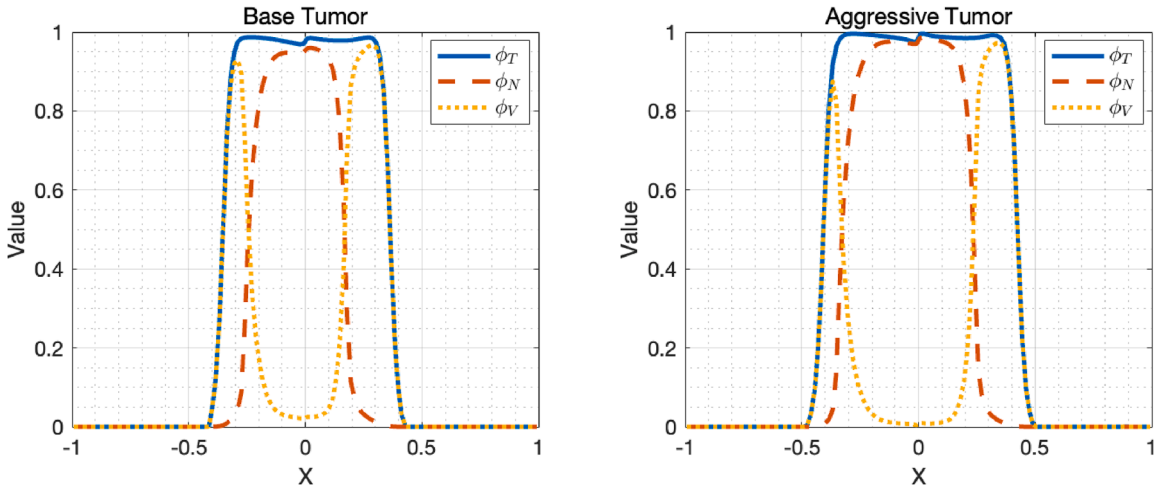

Fig. 12. Cross-sectional profiles at y = 0 for base and aggressive tumors at T = 10.

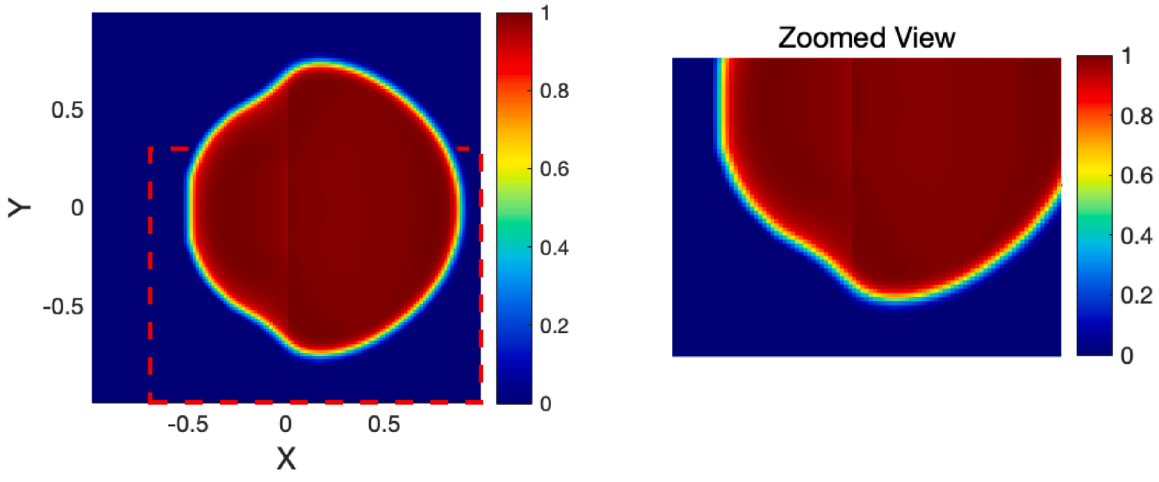

Fig. 13. Morphology of the aggressive tumor at T = 30.

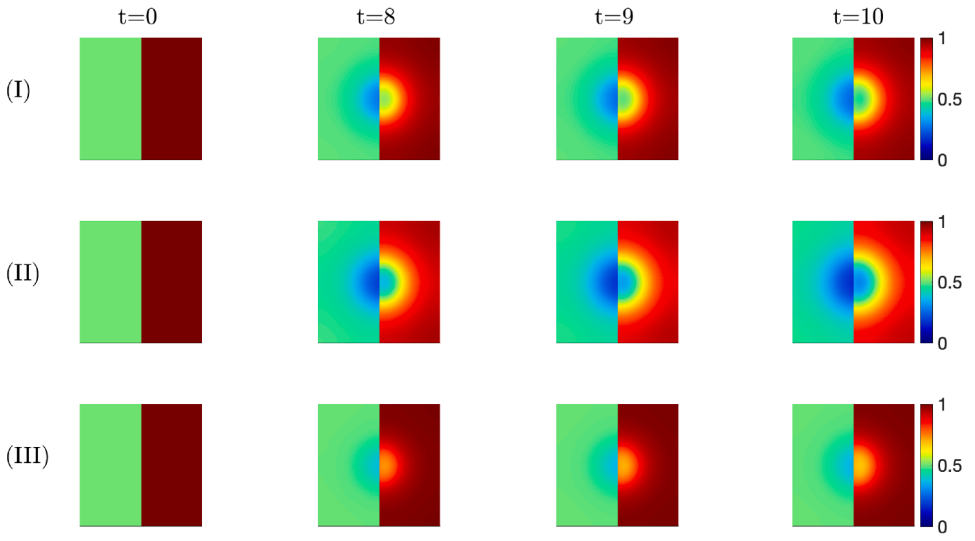

Fig. 14. The evolution of ECM density during tumor growth under different levels of MDE expression: (I) baseline tumor, (II) high MDE expression, (III) low MDE expression.

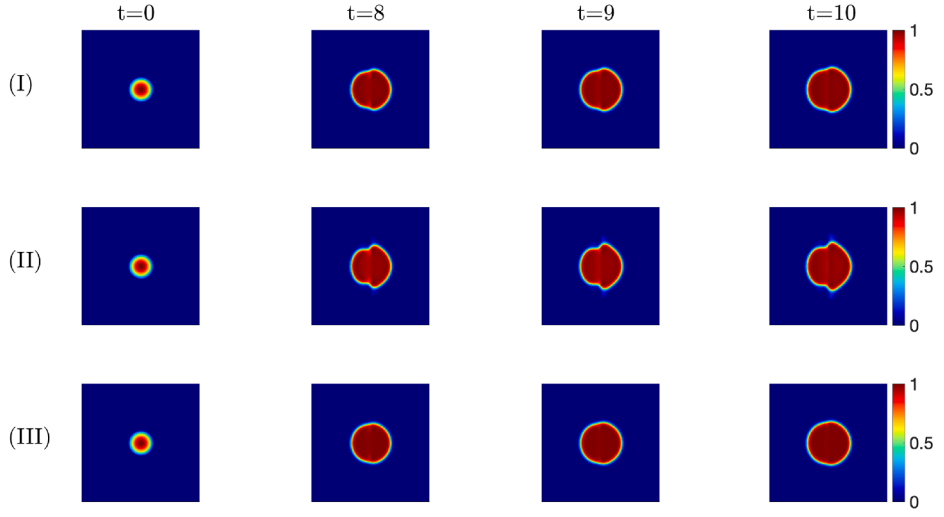

Fig. 15. ϕ_T under different haptotaxis parameters: (I) baseline, (II) high haptotaxis, (III) low haptotaxis parameters to ECM gradients.

characterized by higher MDE decay rates and lower MDE production rates, leading to a smaller difference $|\lambda_M^{\text{pro}}| - |\lambda_M^{\text{dec}}|$, with the parameters for low MDE expression being $\lambda_M^{\text{pro}} = 0.5$ and $\lambda_M^{\text{dec}} = 1.5$.

In Fig. 14, the evolution of ECM density during tumor growth under different levels of MDE expression is illustrated. The second and third rows imply that high MDE expression leads to more significant ECM degradation, while low MDE expression results in weaker ECM degradation. This dynamic interaction influences the ECM degradation process and affects the tumor microenvironment.

We now investigate the effects of different haptotaxis parameters χ_H on tumor volume fraction growth. Fig. 15 displays the tumor evolution under different haptotaxis parameters: a baseline tumor with $\chi_H = 0.001$, a low haptotaxis parameter with $\chi_H = 0.0005$, and a high haptotaxis parameter with $\chi_H = 0.002$. Compared to the baseline tumor, the tumor with a low haptotaxis parameter adopts a more circular shape and exhibits lower sensitivity to the ECM gradient. In contrast, with a high haptotaxis parameter, the tumor shape forms a bump along the vertical axis. As shown in Fig. 15, with the increase in the haptotaxis parameter, tumor cells may become more sensitive to the ECM density gradient and could tend to migrate along regions with greater variations in ECM density.

Remark 4. Although a quantitative comparison is not yet feasible due to the lack of available experimental data, our simulation results show good qualitative agreement with experimental observations. In particular, our model predicts the development of a layered tumor structure featuring a central necrotic core surrounded by a rim of viable cells. This simulated morphology is consistent with experimental findings in the literature. For example, Egloff-Juras et al. [47] reported that in the FaDu spheroid slice, by day 7, "the necrotic core began to appear, while the proliferative cells were mainly located on the periphery of the spheroid". Hirschhaeuser

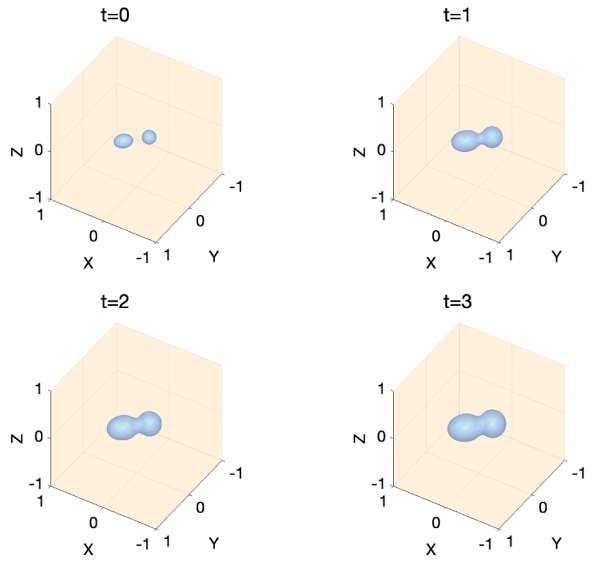

Fig. 16. Volume fraction simulation of ϕ_T within a three-dimensional domain $\Omega = (-1, 1)^3$, with isosurfaces at a volume fraction of 0.8 shown at $t = \{0, 1, 2, 3\}$.

et al. [46] presented the FaDu spheroid slice (corresponding to Fig. 3c in [46]), which illustrates "the typical architecture of a multicellular tumor spheroid with an outer viable rim and a necrotic core".

4.3. Three-dimensional simulations

To further demonstrate the applicability of our method to more complex problems, we present 3D simulations. In the three-dimensional computation, we consider two distinct, separated ellipsoidal tumor volume fractions as initial conditions. In terms of the first tumor volume fraction, we define a spherical region centered at $(-0.15, -0.15, 0)$ and calculate the volume fraction using the following function:

$$\phi_{T_{ball}}(x, y, z) = \exp\left(1 - \frac{1}{1 - 16((x + 0.15)^2 + (y + 0.15)^2 + z^2)}\right). \tag{4.3}$$

Regarding the second tumor volume fraction, we rotate the coordinates, define an ellipsoidal region centered at $(0.15, 0.15, 0)$, and calculate the volume fraction using the following function:

$$\phi_{T_{elliptic}}(x, y, z) = \exp\left(1 - \frac{1}{1 - 16((x_{rot})^2 + (y_{rot}/1.35)^2 + z^2)}\right), \tag{4.4}$$

where (x_{rot}, y_{rot}) is obtained by rotating $(x - 0.15, y - 0.15)$ using a rotation matrix defined as:

$$\begin{bmatrix} \cos(\gamma) & -\sin(\gamma) \\ \sin(\gamma) & \cos(\gamma) \end{bmatrix}, \quad \text{with } \gamma = \frac{\pi}{4}. \tag{4.5}$$

Finally, we add these two tumor volume fractions to obtain the total tumor volume fraction

$$\phi_T = \phi_{T_{ball}} + \phi_{T_{elliptic}}. \tag{4.6}$$

At the initial time, the nutrient concentration ϕ_σ throughout the domain is set to 1, the MDE volume fraction ϕ_M is initialized to 0, and the ECM density θ is also initialized using the ring structure, similar to the profile (4.2) in the 2D simulation.

We take a numerical resolution $N_x = N_y = N_z = 128$ and the time step size of $\tau = 8 \times 10^{-3}$. Fig. 16 illustrates the evolution of tumor cell volume fractions within the three-dimensional domain $\Omega = (-1, 1)^3$. These isosurfaces clearly depict the growth and expansion of the tumor over time. It is observed that the tumors begin to connect at $t = 2$; as time progresses, the conjoined tumor volume fraction becomes larger.

Our simulation results have provided visualizations of the tumor growth model. In addition, the presented numerical examples have also offered a clear understanding of how different biological factors influence tumor growth dynamics, and these results may assist in the prediction of tumor progression.

5. Conclusion

This research proposes a numerical approach to simulate a tumor growth model, emphasizing the degradation of the ECM. This model incorporates various biological elements, including tumor cells, viable cells, necrotic cells, and the evolution of MDE and ECM.

The main contributions of this work are fourfold. First, we have developed a decoupled, linear, explicit, and easily solvable algorithm. The algorithm exhibits excellent properties in terms of the MBP and bound preserving, with a theoretical proof. Second, the numerical algorithm employs a cut-off only for the variable ϕ_T, while the remaining four variables automatically maintain the MBP and bound preserving properties. As a result, the computation adheres to the physical properties at the discrete level. In comparison, the method in an existing work [18] applies a cut-off function to all variables in the original equations. This ensures that the values inserted into the equations at each time step remain bounded within the given time interval. However, a theoretical proof of the bound preservation for this method throughout the entire computation process would face certain difficulties.

Third, we simulated tumor growth under different initial ECM conditions and explored the effects of nutrient supply, variations in MDE expression levels on ECM degradation, as well as the influence of different haptotaxis parameters on tumor growth. Finally, for the ETDRK scheme, we accelerated the computation using FFT-based DCT. In the presented 3D simulation ($N = 128$, $\tau = 8 \times 10^{-3}$, and $T = 3$), we used a MacBook Pro-14 with an Apple M1 Pro-chip and 16GB of RAM. This computation, implemented in MATLAB and completed in a total elapsed wall-clock time of 613.69 seconds, has demonstrated high efficiency.

Several limitations have also been observed in this study. First, due to the highly nonlinear and strongly coupled nature of the model, only qualitative analyses have been conducted so far, without systematic quantitative comparison. In future work, we aim to develop comprehensive parameter sensitivity analyses and introduce standardized quantitative metrics to gain deeper insights into tumor progression dynamics. Moreover, to obtain the numerical MBP of the Cahn-Hilliard-type equations, a cut-off strategy is adopted in this study. As an alternative, we plan to explore logarithmic-type energy potential, which naturally leads to a positivity-preserving formulation (see [34]), thus avoiding nonphysical solution.

In future research, our objective is also to explore the impact of angiogenesis on tumor growth and to consider specific cancers and drug therapies in the model. In conclusion, this research provides promising insights for the advancement of clinical research in cancer and enhances the understanding of tumor growth dynamics.

CRediT authorship contribution statement

Qiumei Huang: Writing – review & editing, Validation, Supervision, Project administration; **Zhonghua Qiao:** Writing – review & editing, Supervision, Project administration, Methodology; **Cheng Wang:** Writing – review & editing, Validation, Supervision, Project administration; **Huiting Yang:** Writing – original draft, Visualization, Methodology, Formal analysis.

Data availability

Data will be made available on request.

Declaration of competing interest

The authors declare that they have no known competing financial interests or personal relationships that could have appeared to influence the work reported in this paper.

Acknowledgments

Q. Huang's work is supported by the National Natural Science Foundation of China (No.12371385); Z. Qiao's work is partially supported by the CAS AMSS-PolyU Joint Laboratory of Applied Mathematics (No. JLFS/P-501/24) and the Hong Kong Research Grants Council RFS grant RFS2021-5S03, GRF grants 15302122 and 15305624; C. Wang's work is supported by the National Science Foundation (DMS 2012269, DMS 2309548).

References

[1] H. Sung, J. Ferlay, R.L. Siegel, M. Laversanne, I. Soerjomataram, A. Jemal, F. Bray, Global cancer statistics 2020: GLOBOCAN estimates of incidence and mortality worldwide for 36 cancers in 185 countries, CA Cancer J. Clin. 71 (3) (2021) 209–249.
[2] P. Lu, V.M. Weaver, Z. Werb, The extracellular matrix: a dynamic niche in cancer progression, J. Cell Biol. 196 (4) (2012) 395–406.
[3] T.R. Cox, The matrix in cancer, Nat. Rev. Cancer. 21 (4) (2021) 217–238.
[4] E. Henke, R. Nandigama, S. Ergün, Extracellular matrix in the tumor microenvironment and its impact on cancer therapy, Front. Mol. Biosci. 6 (2020) 160.
[5] D.H. Madsen, T.H. Bugge, The source of matrix-degrading enzymes in human cancer: problems of research reproducibility and possible solutions, J. Cell Biol. 209 (2) (2015) 195–198.
[6] M.A.J. Chaplain, M. Lachowicz, Z. Szymanska, D. Wrzosek, Mathematical modelling of cancer invasion: the importance of cell–cell adhesion and cell–matrix adhesion, Math. Models Methods Appl. Sci. 21 (04) (2011) 719–743.
[7] Y.T. Nguyen Edalgo, A.N. Ford Versypt, Mathematical modeling of metastatic cancer migration through a remodeling extracellular matrix, Processes 6 (5) (2018) 58.
[8] N. Sfakianakis, A. Madzvamuse, M.A.J. Chaplain, A hybrid multiscale model for cancer invasion of the extracellular matrix, Multiscale Model. Simul. 18 (2) (2020) 824–850.
[9] X. Zheng, K. Zhao, T. Jackson, J. Lowengrub, Tumor growth towards lower extracellular matrix conductivity regions under Darcy's law and steady morphology, J. Math. Biol. 85 (1) (2022) 5.
[10] B. Blanco, R. Palma, M. Hurtado, G. Jiménez, C. Griñán-Lisón, J. Melchor, J.A. Marchal, H. Gomez, G. Rus, J. Soler, Modeling low-intensity ultrasound mechanotherapy impact on growing cancer stem cells, Math. Comput. Simul. 228 (2025) 87–102.
[11] X. Wu, G.J. Van Zwieten, K.G. Van der Zee, Stabilized second-order convex splitting schemes for Cahn-Hilliard models with application to diffuse-interface tumor-growth models, Int. J. Numer. Methods Biomed. Eng. 30 (2) (2014) 180–203.

[12] J. Xu, G. Vilanova, H. Gomez, Full-scale, three-dimensional simulation of early-stage tumor growth: the onset of malignancy, Comput. Methods Appl. Mech. Eng. 314 (2017) 126–146.
[13] J. Xu, G. Vilanova, H. Gomez, Phase-field model of vascular tumor growth: three-dimensional geometry of the vascular network and integration with imaging data, Comput. Methods Appl. Mech. Eng. 359 (2020) 112648.
[14] G. Lorenzo, A.S. Michael, K. Tew, J.R.H. Thomas, H. Gomez, Hierarchically refined and coarsened splines for moving interface problems, with particular application to phase-field models of prostate tumor growth, Comput. Methods Appl. Mech. Eng. 319 (2017) 515–548.
[15] P. Colli, H. Gomez, G. Lorenzo, G. Marinoschi, A. Reali, E. Rocca, Mathematical analysis and simulation study of a phase-field model of prostate cancer growth with chemotherapy and antiangiogenic therapy effects, Math. Models Methods Appl. Sci. 30 (07) (2020) 1253–1295.
[16] V. Mohammadi, M. Dehghan, Simulation of the phase field Cahn-Hilliard and tumor growth models via a numerical scheme: element-free Galerkin method, Comput. Methods Appl. Mech. Eng. 345 (2019) 919–950.
[17] M. Fritz, P.K. Jha, T. Köppl, J.T. Oden, B. Wohlmuth, Analysis of a new multispecies tumor growth model coupling 3D phase-fields with a 1D vascular network, Nonlinear Anal. Real World Appl. 61 (2021) 103331.
[18] M. Fritz, E.A. Lima, V. Nikolić, J.T. Oden, B. Wohlmuth, Local and nonlocal phase-field models of tumor growth and invasion due to ECM degradation, Math. Models Methods Appl. Sci. 29 (13) (2019a) 2433–2468.
[19] M. Fritz, E.A. Lima, J. Tinsley Oden, B. Wohlmuth, On the unsteady Darcy–Forchheimer–Brinkman equation in local and nonlocal tumor growth models, Math. Models Methods Appl. Sci. 29 (09) (2019b) 1691–1731.
[20] A. Hawkins-Daarud, K.G. van der Zee, J. Tinsley Oden, Numerical simulation of a thermodynamically consistent four-species tumor growth model, Int. J. Numer. Methods Biomed. Eng. 28 (1) (2012) 3–24.
[21] E.A.B.F. Lima, J.T. Oden, R.C. Almeida, A hybrid ten-species phase-field model of tumor growth, Math. Models Methods Appl. Sci. 24 (13) (2014) 2569–2599.
[22] L. Ju, X. Li, Z. Qiao, J. Yang, Maximum bound principle preserving integrating factor Runge-Kutta methods for semilinear parabolic equations, J. Comput. Phys. 439 (2021) 110405.
[23] J. Feng, Y. Zhou, T. Hou, A maximum-principle preserving and unconditionally energy-stable linear second-order finite difference scheme for Allen–Cahn equations, Appl. Math. Lett. 118 (2021) 107179.
[24] H. Zhang, X. Qian, S. Song, Third-order accurate, large time-stepping and maximum-principle-preserving schemes for the Allen-Cahn equation, Numer. Algorithms (2023a) 1–38.
[25] H. Zhang, J. Yan, X. Qian, S. Song, Temporal high-order, unconditionally maximum-principle-preserving integrating factor multi-step methods for Allen-Cahn-type parabolic equations, Appl. Numer. Math. 186 (2023b) 19–40.
[26] Q. Du, L. Ju, X. Li, Z. Qiao, Maximum principle preserving exponential time differencing schemes for the nonlocal Allen–Cahn equation, SIAM J. Numer. Anal. 57 (2) (2019) 875–898.
[27] Q. Du, L. Ju, X. Li, Z. Qiao, Maximum bound principles for a class of semilinear parabolic equations and exponential time-differencing schemes, SIAM Rev. 63 (2) (2021) 317–359.
[28] Q. Huang, Z. Qiao, H. Yang, Maximum bound principle and non-negativity preserving ETD schemes for a phase field model of prostate cancer growth with treatment, Comput. Methods Appl. Mech. Eng. 426 (2024) 116981.
[29] M. Fritz, Tumor evolution models of phase-field type with nonlocal effects and angiogenesis, Bull. Math. Biol. 85 (6) (2023) 44.
[30] M.A.J. Chaplain, G. Lolas, Mathematical modelling of cancer invasion of tissue: dynamic heterogeneity, Netw. Heterog. Media 1 (3) (2006) 399–439.
[31] Y. Tao, M. Winkler, A chemotaxis-haptotaxis model: the roles of nonlinear diffusion and logistic source, SIAM J. Numer. Anal. 43 (2) (2011) 685–704.
[32] N. Nargis, R. Aldredge, Effects of matrix metalloproteinase on tumour growth and morphology via haptotaxis, J. Bioengineer. & Biomedical Sci 6 (2016) 1000207.
[33] C. Liu, Z. Qiao, Q. Zhang, Two-phase segmentation for intensity inhomogeneous images by the Allen-Cahn local binary fitting model, SIAM J. Sci. Comput. 44 (1) (2022) B177–B196.
[34] W. Chen, C. Wang, X. Wang, S.M. Wise, Positivity-preserving, energy stable numerical schemes for the Cahn-Hilliard equation with logarithmic potential, J. Comput. Phys. X 3 (2019) 100031.
[35] S.M. Wise, Unconditionally stable finite difference, nonlinear multigrid simulation of the Cahn-Hilliard-Hele-Shaw system of equations, J. Sci. Comput. 44 (1) (2010) 38–68.
[36] K. Cheng, W. Feng, C. Wang, S.M. Wise, An energy stable fourth order finite difference scheme for the Cahn-Hilliard equation, J. Comput. Appl. Math. 362 (2019) 574–595.
[37] D. Li, Z. Qiao, T. Tang, Characterizing the stabilization size for semi-implicit fourier-spectral method to phase field equations, SIAM J. Numer. Anal. 54 (2016) 1653–1681.
[38] D. Li, Z. Qiao, On second order semi-implicit fourier spectral methods for 2D Cahn-Hilliard equations, J. Sci. Comput. 70 (2017) 301–341.
[39] Y. Yan, W. Chen, C. Wang, S.M. Wise, A second-order energy stable BDF numerical scheme for the Cahn-Hilliard equation, Commun. Comput. Phys. 23 (2018) 572–602.
[40] P. Hartman, Ordinary Differential Equations, SIAM, 2002.
[41] K. Cheng, Z. Qiao, C. Wang, A third order exponential time differencing numerical scheme for no-slope-selection epitaxial thin film model with energy stability, J. Sci. Comput. 81 (1) (2019) 154–185.
[42] X. Meng, Z. Qiao, C. Wang, Z. Zhang, Artificial regularization parameter analysis for the no-slope-selection epitaxial thin film model, CSIAM Trans. Appl. Math. 1 (3) (2020) 441–462.
[43] C. Van Loan, Computational Frameworks for the Fast Fourier Transform, SIAM, 1992.
[44] J. Winkler, A. Abisoye-Ogunniyan, K.J. Metcalf, Z. Werb, Concepts of extracellular matrix remodelling in tumour progression and metastasis, Nat. Commun. 11 (1) (2020) 5120.
[45] A. Lo Cicero, S. Campora, G. Lo Buglio, P. Cinà, M. Lo Pinto, S.D. Scilabra, G. Ghersi, Enhancing therapeutic efficacy through degradation of endogenous extracellular matrix in primary breast tumor spheroids, FEBS J. (2025).
[46] F. Hirschhaeuser, H. Menne, C. Dittfeld, J. West, W. Mueller-Klieser, L.A. Kunz-Schughart, Multicellular tumor spheroids: an underestimated tool is catching up again, J. Biotechnol. 148 (1) (2010) 3–15.
[47] C. Egloff-Juras, I. Yakavets, V. Scherrer, A. Francois, L. Bezdetnaya, H.-P. Lassalle, G. Dolivet, Validation of a three-dimensional head and neck spheroid model to evaluate cameras for NIR fluorescence-guided cancer surgery, Int. J. Mol. Sci. 22 (4) (2021) 1966.